Research Article
DOI: http://dx.doi.org/10.2110/jsr.2017.15
THE TRANSFORMATION OF SEDIMENT INTO ROCK: INSIGHTS FROM IODP SITE U1352, CANTERBURY BASIN, NEW ZEALAND

KATHLEEN M. MARSAGLIA,[1] GREG H. BROWNE,[2] SIMON C. GEORGE,[3] DAVID B. KEMP,[4] JOHN M. JAEGER,[5] DAVID CARSON,[1] MATHIEU RICHAUD,[6] AND IODP EXPEDITION 317 SCIENTIFIC PARTY
[1] Department of Geological Sciences, California State University, Northridge, Northridge, California, 91330-8266, U.S.A.
[2] GNS Science, 1 Fairway Drive, 5010 Lower Hutt, New Zealand
[3] Department of Earth and Planetary Sciences and Macquarie University Marine Research Centre, Macquarie University, Sydney, New South Wales 2109, Australia
[4] School of Geosciences, University of Aberdeen, Old Aberdeen AB24 3UE, U.K.
[5] Department of Geological Sciences, University of Florida, Gainesville, Florida 32611-2120, U.S.A.
[6] Department of Earth and Environmental Sciences, California State University, Fresno, California 93740, U.S.A.
e-mail: kathie.marsaglia@csun.edu
ABSTRACT: At Integrated Ocean Drilling Program (IODP) Expedition 317 Site U1352, east of the South Island New Zealand, we continuously cored a 1927-m-thick Holocene-to-Eocene section where we can uniquely document downhole changes in induration and lithification in siliciclastic to calcareous fine-grained sediment using a wide range of petrological, physical-property, and geochemical data sets. Porosity decreases from around 50% at the surface to 5–10% at the base of the deepest hole, with a corresponding increase in density from ~ 2 to ~ 2.5 g cm^3. There are progressive bulk mineral changes with depth, including an increase in carbonate and decrease in quartz and clay content. Grain compaction is first seen in thin section at 347 m below sea floor and intensifies downhole. Pressure solution (chemical compaction) begins at 380 m and is common below 1440 m, with stylolite development below 1600 m, and sediment injection features below 1680 m. Porewater geochemistry and petrographic observations document two active zones of cementation, one shallow (eogenetic) down to ~ 50 m, as evidenced by micritic nodules and pore-water geochemistry driven by methane oxidation by sulfate, and another burial-related cementation zone (mesogenetic) starting at ~ 300 m. A transitional zone occurs between 50 and 300 m. Our results quantify downhole diagenetic changes and verify depth estimates for these processes inferred from outcrop studies, and provide an actualistic example of cementation and compaction trends in a slope setting.

INTRODUCTION

Although the fundamental processes by which sediments lithify are well known (Morse and Mackenzie 1990; Burley and Worden 2003; Armenteros 2010), relatively few studies have documented the sediment-to-rock transition with depth based on a continuously cored borehole record in fine-grained continental-margin settings, and none, to our knowledge, have linked this transition to both physical-property and porewater-

geochemistry data. Previous studies utilizing outcrop and borehole data have been limited by outcrop scale, weathering, and borehole conditions. Regarding siliciclastic systems, these studies have concentrated either on shallow-burial (Galloway 1984) or deeper-burial (> 1000 m) settings (Paxton et al. 2002). The classic carbonate study is based on sets of data from shallow-water carbonate successions in Florida that are semicontinuous from the surface to ~ 5 km burial depth, with porosities derived only from borehole logging data (Schmoker and Halley 1982; Halley and Schmoker 1983). Cementation and diagenetic changes at intermediate burial depths (hundreds of meters) are less well understood, in part because their burial histories have been largely inferred from outcrop studies (Nelson et al. 1988; Morse and Mackenzie 1990; Nicolaides 1995; Stone and Siever 1996; Nicolaides and Wallace 1997; Fabricius and Borre 2007). Deep-burial carbonate diagenesis in marine basins has been discussed in detail by Choquette and James (1987), including aspects of physical (reorientation and compression of components) and chemical (stylolites, microstylolites, and fitted fabrics) compaction.

In 2009, Integrated Ocean Drilling Program (IODP) Expedition 317 drilled and continuously cored Site U1352 on the eastern margin of the South Island, New Zealand (Fig. 1). The drill site, (44° 56.2′ S, 172° 01.3′ E) is located 70 km east of the coastline with a water depth of 349 m on the upper slope of the Canterbury continental shelf margin. The site was drilled to a total depth of 1927 m (core depth below seafloor CSF-A) at a combination of four closely spaced (within tens of meters of each other) holes (U1352A, B, C, D), with Hole U1352C having the deepest penetration. Unless otherwise noted, all depths are reported in meters (CSF-A), with an average of 63% core recovery (Fig. 2; Fulthorpe et al. 2011). U1352C is one of the deepest sedimentary drill holes in over forty years of deep-sea exploration by the Deep Sea Drilling Project (DSDP), the Ocean Drilling Program (ODP), and the Integrated Ocean Drilling Program (IODP) combined, and one of only a handful of continuously cored sites to penetrate over 1500 m below the seafloor. In addition to this drill hole, there are several nearby offshore petroleum exploration wells (e.g., Clipper-1, Resolution-1, and Galleon-1) that targeted more deeply buried intervals at depths of > 3,000 m (Fig. 1). These, like most industry wells around the world, provide only limited information about the upper 2,000 m of continental margin stratigraphy and processes of lithification, by way of sporadic cuttings samples and electric logs.

Petrologic, stratigraphic, physical-property, and geochemical data amassed from Site U1352 offer unique insights into the sediment-to-rock transition in an ~ 2-km-thick Holocene-to-Eocene passive-margin succession (Fulthorpe et al. 2011). The overall regressive continental-slope sequence comprises a mix of carbonate and siliciclastic mud(stone), sandy marl(stone) (marl is 30–70% carbonate, after Shipboard Scientific Party 2004), micrite, and minor sand(stone) that reflect the increasing input of siliciclastic sediment in the Neogene (Fig. 2). The terrigenous sediment components are derived largely from basement source areas dominated by Torlesse and Caples sandstone and mudstone and their metamorphic equivalents (schist) of the South Island, supplied from the active, obliquely convergent Australian–Pacific plate boundary (Browne and Naish 2003; Lu et al. 2003).

Here, we summarize a multidisciplinary sedimentological, mineralogical, petrophysical, and geochemical shipboard dataset of over 1400 meters of core recovered

at Site U1352 coupled with targeted post-expedition geochemical and petrologic studies that interpret the progressive lithification processes occurring in marine continental-slope stratigraphic successions with mixed siliciclastic–calcareous compositions.

GEOLOGIC SETTING

The offshore Canterbury Bight region represents a passive margin developed initially during mid-Cretaceous rifting of eastern Gondwana, followed by a Late Cretaceous and Paleogene drift phase (Carter and Norris 1976; Field and Browne 1989). During the Neogene, increased plate convergence between the Australian and Pacific plates developed into a strongly oblique plate convergence zone through the South Island, resulting in the uplift of the Southern Alps and evolution of the Alpine Fault (Wellman 1979; Adams 1980; Tippett and Kamp 1993; Sutherland et al. 2000). Neogene sediments at Site U1352 were ultimately derived from the uplift of the Southern Alps, and reflect a range of depositional and diagenetic processes. Despite having been adjacent to the tectonically active central South Island and Southern Alps throughout the period of deposition, the sediments at Site U1352 are largely fine-grained with less abundant sand(stone). Oligocene–Miocene strata are calcareous, and there is increasing siliciclastic input through the Neogene. They reflect a subsiding basin receiving an increasing supply of fine-grained sediment from the eroding hinterland, transported via fluvial and shelf processes to the slope, albeit with fluctuations due to sea-level change, climate, and changing volumes and delivery mechanisms of sediment to the depocenter. Some of these factors have been described by other workers for the Canterbury margin (Browne and Naish 2003; Lu and Fulthorpe 2004; Villasenor et al. 2015).

The oldest sediment penetrated at Site U1352 is a pelagic late Eocene micritic limestone: the Amuri Limestone (Browne and Field 1985). A significant (~ 12 My unconformity, the Marshall Paraconformity (also known as the Marshall Unconformity), separates the early Oligocene (30–32 Ma) Amuri Limestone from overlying early Miocene (~ 18–19 Ma) sediments (Field and Browne 1989; Fulthorpe et al. 2011). This unconformity at Site U1352 was represented by the drilling of fragments of darker (phosphatized) limestone, but in outcrop in the adjacent South Island the same interval is marked by intensely bioturbated glauconitic sandstone infilling a burrowed and phosphatized unconformity surface (Carter and Landis 1972 1982; Findlay 1980; Carter 1985; Lever 2007).

The overlying lower Miocene is represented mostly by marls, muddy sands, sandy muds, and mud deposits developed as a series of sediment drifts (Fulthorpe and Carter 1991; Lu et al. 2003; Lu and Fulthorpe 2004; Carter 2007). These slope sediments were sourced from the south by contour-parallel flows deposited under the influence of the north-traveling Subantarctic Mode Water (SAMW) and Intermediate Water (AAIW), and their predecessor current systems (Sutton 2003; Carter and Gammon 2004). Younger Pliocene to Quaternary sediments of Site U1352 represent largely pelagic and hemipelagic muds, intercalated with sandy units episodically fed by a combination of across-shelf, delta-front (Quaternary), and along-slope contour-current (Pliocene) processes. These sediments are derived from South Island greywacke sources of the Canterbury hinterland immediately to the west (the Torlesse and Caples terranes), and from schist-dominated terranes to the south (the Haast Schist basement terrane)

representing largely metamorphosed graywacke (Fulthorpe et al. 2011; Bender-Whitaker 2013; Villasenor et al. 2015; Bailey, unpublished data).

METHODS

Four holes, offset horizontally by 20 m from each other, were drilled at Site U1352 using three continuous coring techniques (see Methods in Fulthorpe et al. 2011 for further information): Hole U1352A, advance piston-cored (APC) from 0 to 42.2 m drilling depth below seafloor (DSF); Hole U1352B, APC extended core barrel (XCB) from 0 m (DSF) until refusal at 830.9 m (DSF); Hole U1352C, rotary core barrel (RCB) from 631.1 m DSF to the total depth of 1927.5 m (DSF). Hole U1352D was drilled by APC to provide a further record of the uppermost 127 m (DSF). Integrated Ocean Drilling Program engineers have found that this combination of techniques maximizes core recovery and minimizes core disturbance as the strata become increasingly compacted and lithified with depth.

Aboard ship, the 1443.65 m of 7-cm-diameter core recovered within the 1927.5 m cored interval at Site U1352 was cut into sections of 1.5 m or less, split, and visually described, noting sedimentary structures, bedding features, bioturbation, Munsell color, drilling disturbance, and lithology, as described in Fulthorpe et al. (2011). See the Methods section of Fulthorpe et al. (2011) for details on lithofacies description procedures. Lithologic composition was determined at sea through petrographic examination of 442 smear slides and 67 thin sections prepared shipboard from selected intervals (see http://publications.iodp.org/proceedings/317/EXP_REPT/CORES/SS_U1352.PDF for compositional data determined shipboard for these samples, and additional information in Carson and Marsaglia 2015). Samples are identified by Hole#-Core#-Section# and cm interval. Observations of porosity in shipboard thin sections made with clear epoxy were limited by the effects of plucking during fabrication, but a more extensive suite of thin sections prepared using vacuum impregnation with blue-dyed epoxy for Carson and Marsaglia (2015) provided clear definition and facilitated visual quantification of interparticle and intraparticle porosity. The stratigraphic and core-recovery columns in Figure 2 are based on coring results from Holes U1352B (top) and U1352C (bottom), for a total of 1195 m of recovered core over a depth range of 1927.5 m. Note that when core recovery is incomplete, the IODP convention is to move all core to the top of the cored interval.

One hundred and twelve interstitial water samples were collected and analyzed at Site U1352. See the Methods section of Fulthorpe et al. (2011) for details of sample collection and analysis. The water samples were extracted from 10–30 cm segments cut from the core (whole-rounds) removed directly after core recovery and before further processing, including slabbing. Thirty-one samples were taken from Hole U1352A, then between one and three samples per core down to 300 m, after which alternate cores or spot samples were taken down to 1000 m. Below 1000 m, sampling for interstitial water was irregular, and some whole-round samples as long as 30 cm failed to yield any water for analysis. The amount of interstitial water extracted from whole-round samples decreased with depth from ~ 2 to 5 mL/cm in the first 700 m to < 1 mL/cm in depths below 900 m (Fig. 3). The deepest whole-round sample to yield interstitial water, from a depth of 1386 m, produced 0.5 mL/cm.

On-board analyses of interstitial water followed the procedures outlined by Gieskes et al. (1991) and Murray et al. (2000), as modified for the expedition (see the Methods section in Fulthorpe et al. 2011). Salinity was measured with a Reichert temperature-compensated manual refractometer, previously calibrated using the International Association for the Physical Sciences of the Oceans (IAPSO) seawater standard. Alkalinity and pH were measured immediately after squeezing by Gran titration with a Metrohm autotitrator. Alkalinity is defined as the number of moles of hydrogen ions required to titrate the excess base (alkalinity) in the solution (Gieskes et al. 1991). The IAPSO seawater standard was used for the standardization of alkalinity. Variation for alkalinity was 2–3% based on the IAPSO standard run after every fifth sample. Concentrations of sulfate, chloride, magnesium, calcium, sodium, and potassium in interstitial water were determined with a Dionex ICS-3000 ion chromatograph on 1:200 diluted aliquots in 18 MΩ water. The IAPSO seawater standard was used to standardize measurements made on the ion chromatograph by running it after every fifth sample. The coefficient of variation based on seven repeat analyses of a sample of interstitial water for anions and cations measured on the ion chromatograph was 0.002%. Any batches of samples with > 2% drifts for the IAPSO standard were rerun.

Additional mineralogical (X-ray diffraction), physical properties (color, discrete-sample moisture and density (MAD), porosity and bulk density, magnetic susceptibility, and natural gamma radiation), geochemical (pore-water chemistry, organic and inorganic geochemistry), and biostratigraphic techniques were applied to the cores (for details see Fulthorpe et al. 2011). Porosity was determined from ~ 10 cm^3 samples selected from the middle of each ~ 1.5 m core section by measurements of wet sediment mass and volume and/or dry sediment mass and volume using techniques described in Fulthorpe et al. (2011). Downhole wire-line logging was conducted, but casing of the upper 100 m and obstructions in the hole limited the wireline data to 100–475 m DSF (for details see Fulthorpe et al. 2011). Shipboard analyses are summarized in Figures 2 and 3 and integrated herein with additional post-expedition observations from thin sections vacuum-impregnated with blue epoxy, carbon and oxygen isotopic analysis, X-ray diffraction, and SEM backscatter imaging (see Methods in Carson and Marsaglia 2015).

RESULTS

Lithology Trends with Depth

Three lithostratigraphic units are recognized at Site U1352, named Units I, II, and III, in turn subdivided further into subunits (e.g., A, B, C) (Fig. 2; for details on units and subunits see Fulthorpe et al. 2011). Thin sections created shipboard and for other post-cruise studies provide information on the downhole distribution of sediment components, authigenic phases including carbonate cement, pressure solution at grain contacts and along seams, as well as stylolites and sediment injection features (Fig. 2). These features are illustrated in core photos (Fig. 4) and thin-section photomicrographs (Fig. 5) and are discussed below, where we summarize observations made during drilling and post-expedition.

Holocene to early Pliocene–age Unit I (0–710 m) is homogenous, poorly lithified bioturbated siliciclastic mud and sandy marl, with sand interbeds in the upper 100 m. Other than mollusk shells and thin micritic horizons and nodules, the unit is largely noncalcareous and nonlithified. Subunit IA (0 to 98.4 m) is a mottled gray poorly lithified

mud that contains a small proportion of dispersed very fine sand–size material, thin clay intervals, and thin gray-colored very fine- to fine-grained sand. These lithologies contain varying amounts of shelly material; bivalve, gastropod, barnacle, bryozoan, and worm tube fragments are common shell types. At ~ 10 m there are carbonate-cemented nodules (Fig. 4) composed of mainly authigenic dolomite with $\delta^{13}C$ and $\delta^{18}O$ isotopic values of –20.4‰ VPDB and 6.7‰ VPDB, respectively (details in Carson and Marsaglia 2015). Subunit IB (98.4 to 446.9 m) is a gray to greenish gray mud, with rare to locally abundant shells, and decimeter-thick sand, sandy mud, muddy sand, and marl. It is distinguished from Subunit IA above by the lack of gray sand beds and the presence of greenish gray marl. Cemented nodules are present in the greenish gray sandy muds and muddy sands. For example, a lithified interval of sandy foram-rich marlstone at ~ 300 m exhibits minor (2%) micrite (calcite?) cement localized in foraminifer tests. The sparse nodules are bioturbated micritic marlstone (muddy carbonate) with minor terrigenous silt and sand, organic debris, and bioclasts, including echinoderm fragments, degraded and micritized foraminifers, and molds of mollusks (~ 150 m; see Carson and Marsaglia 2015). Pyrite is present as minor cement (Fig. 5A, B) locally concentrated within burrows and moldic pores. Some foraminifers in this subunit are micritized and show distinctive internal overgrowths of fine carbonate crystals. Glauconite is much more prevalent in foraminifer grainstones, occurring as pale green fill of foraminifer tests, darker green discrete pellets with synaeresis cracks, alteration of biotite, as well as some likely epigenetic glauconite in the matrix (Fig. 5G).

The texture in thin sections from this interval ranges from grain supported to matrix supported, with an average visual porosity of ~ 25%, with some zones of foraminifer grainstone ranging as high as 50% total porosity (intraparticle and interparticle) and other matrix-rich areas limited to 15%, mostly intraparticle porosity.

Subunit IC (446.9 to 710.8 m) differs from younger strata by the occurrence of gray-green calcareous muddy sand beds that transition into sandy marl with depth. At the base of this unit the marls contain > 30% carbonate content. Carbonate-cemented intervals increase in frequency and thickness with depth through Subunit 1C. This subunit includes carbonate microfacies slightly different from those described in subunit IB (e.g., Core Samples U1352B-54X-4, 4–6 cm (~ 459 m), -65X-1, 14–17 cm (~ 562 m, pictured in Fig. 4), and U1352C-4R-5, 52–54 cm (~ 600 m)). The carbonate-cemented intervals are finer-grained siliciclastics with a smaller, better-sorted population of bioclasts. The sand fraction is mainly quartz, feldspar (undifferentiated), mica (muscovite with minor biotite), chlorite, and dense minerals. Thin-section samples from this subunit have variable amounts of calcareous matrix and up to 15% carbonate cement. They have no distinct lamination and are somewhat homogenized by bioturbation, with rare large (cm-scale) discrete burrows.

In contrast, the lighter-colored Unit II of early Pliocene to early Miocene age (710–1852 m) is more lithified and more calcareous with intervals of sandy marl(stone), sandy mud(stone), muddy sand(stone), and sandstone. The carbonate component (Fig. 2) is a mix of micrite, nannofossils, sponge spicules, foraminifers, and other shell fragments. Macrofossils such as mollusk shells that are reasonably common in Unit I are either rare or absent in Unit II lithologies. Subunit IIA (710.8 to 1189.3 m) is a dark greenish gray to greenish gray homogeneous sandy marlstone with less lithified sandy marl. Subtly

different facies in Subunit IIA such as paler greenish-gray-colored layers that are generally more cemented, begin to appear at ~ 1026 m and become more common with depth. Alternations of these layers give the rock a color-banded appearance. Lithologies are heavily bioturbated by *Chondrites*, *Helminthopsis*, *Terebellina*, *Scolicia*, *Planolites*, *Zoophycos*, and *Thalassinoides* visible in the more lithified layers. Small (< 1 cm) ovoid crystalline calcareous "blebs" first occur at ~ 970 m, with sporadic occurrences of calcareous concretions. Smear slides indicate that carbonate content, including calcareous biogenic and potential authigenic components, in Unit II varies between 10 and 40% (Fulthorpe et al. 2011). Subunit IIB (1189.3 to 1693.9 m) is a similarly colored marlstone as Subunit IIA, and is distinguished from Subunit IIA above by the common occurrence of thin layers of mudstone (between 1170 and 1392 m), and by the presence of current-bedding features in the marlstone (especially below 1392 m). A banded appearance possibly caused by incipient pressure-solution seams occurs below 1600 m. At 1693 m, darker laminae appear to be depositional features enriched in organic matter and clay minerals.

An increase in cementation is noted with depth in Unit II. Micritized foraminifers show internal carbonate overgrowths. Common micrite may also be authigenic. In the sandy marlstone of Subunit IIB (1189–1693 m) microcrystalline carbonate cement is present throughout, up to 20% as microcrystalline intraparticle cement filling foraminifer chambers, and as interparticle cement in better-sorted grainstone, siltstone, and sandstone laminae and burrow fills. Patchy low-birefringence sulfate (likely barite or celestine) cement is present in Samples U1352C-135R-5, 38–41 cm, -137R-2, 58–60 cm (~1809–1824 m).

The presence of glauconite, as dispersed grains and as discrete layers, distinguishes Subunit IIC (1693.9 to 1852.6 m) from overlying units. The unit contains a variety of lithologies ranging from sandy marlstone to sandy limestone and minor mudstones, to very fine glauconitic sandstone layers, which sometimes crosscut the marlstone to limestone depositional fabric as shown in Figure 4. As discussed below, these crosscutting relationships suggest that glauconitic sand was locally mobilized and injected within the formation.

Minor authigenic quartz (chert), recognized mainly by opaline sponge spicules replaced by birefringent microcrystalline quartz, was not observed until greater depth (Unit II), in thin sections at 1142 m and then at several intervals below at 1250 m, 1390 m, and 1730 m. Additionally, there was patchy silicification and/or replacement and cementation of foraminifers by microcrystalline quartz and chalcedony in sample U1352C-127R-2, 40–43 cm (~ 1730 m).

The oldest Unit III of early Oligocene–late Eocene age (1852–1927 m) is a white to cream-colored indurated micritic limestone (the Amuri Limestone) with abundant stylolites. This unit is distinguished from lithostratigraphic Unit II on the basis of its dominant limestone lithology, color, and induration. An unconformity (the Marshall Unconformity from onshore succession) between lithostratigraphic Units II and III is estimated to represent a 12-million-year hiatus (Fulthorpe et al. 2011). The foraminifer–nannofossil-bearing Amuri Limestone contains minor silt to very fine sand (e.g., quartz, glauconite) and pyrite.

Petrographic Evidence of Compaction with Depth

The first downhole evidence (in thin section) of significant compaction leading to grain alteration occurs in a lithified interval at 347 m (Fig. 4). Microscopic evidence for compaction includes brittle fracturing of fossil fragments and interpenetration (brittle readjustment) of harder grains into softer milliolid foraminifer tests, which are locally preferentially dissolved (Fig. 5). There is often sufficient ultrastructure in the foraminifers to suggest actual preferential (pressure?) dissolution of the milliolid rather than just interpenetration and brittle adjustment. Deeper in the hole (e.g., > 1350 m), compaction is more pronounced.

Evidence for mechanical and chemical compaction is present throughout Subunit IIC starting with grain (bioclast) fracturing, interpenetration, deformation of micrite-filled burrow margins, pressure solution, and development of dark seams and stylolites. Examples of these phenomena are depicted in Figure 5. Locally, there is complete destruction of foraminifer tests (Fig. 5A, B). Muddy burrow fills are compacted and become more ovoid and smeared with depth. Macroscopically, cores show textures similar to those artificially created by Shinn et al. (1977), who progressively compacted carbonate mud. Differential compaction and dissolution also are recognized around dark irregular and stylolitic seams (e.g., 1600 m and 1610 m). The darker intervals (laminae and burrow fills) are potentially associated with organic matter, which appears to enhance chemical compaction, creating darker seams and leading to the formation of stylolites (Fig. 5H) as seen by other workers (see Von Bergen and Carozzi 1990). It is noteworthy that more calcareous samples below this interval show evidence for pressure solution (chemical compaction) only where there is minor organic matter (e.g., 1620 m). The amount of organic matter, mostly < 1.5% TOC throughout the hole (Fulthorpe et al. 2011) declines down section starting in Sample U1352C-137R-2, 58–60 cm (~ 1825 m) down through Unit III.

Trends in Physical Properties with Depth

The general character of the slope sedimentary succession at Site U1352 is fairly homogeneous in Units I and II with few discrete sedimentary structures, and bioturbation is common throughout (Fig. 4). The most fundamental lithological change occurs below the unconformity and in the indurated limestone of Unit III.

In terms of overall sediment-to-rock transitions, the following observations are made (Fulthorpe et al. 2011). Mud transitions to marl (i.e., > 30% carbonate) gradationally below ~ 300 m, and chalk or limestone intervals (i.e., > 70% carbonate) first appear below ~ 1026 m and become more common with depth. Increasing carbonate (combined biogenic and authigenic) and a general reduction in content of clay and quartz with depth are confirmed by shipboard XRD data (Fig. 2), and reflected in decreasing values of natural gamma and magnetic susceptibility and increasing values of grain density (Fig. 2). Discrete-sample porosity values decrease from a broad spread around 50% at the surface (with one value as high as 70%) to 5–10% at the base of the hole (Fig. 2), with a corresponding increase in wet bulk density from around 2 to 2.5 g/cm^3. Across the Unit I–II boundary (700–750 m) there is a sharp decrease in porosity values (Fig. 2), which may relate to a change in the coring method used, but may also relate to changes in compaction and carbonate cementation, as outlined below. This progressive lithification, from largely unconsolidated to well lithified, can be seen in Figure 4, in examples of core segments sampled by piston (H) to extended core barrel (X) to rotary core (R) methods

with increased depth and induration (see Operations section in Fulthorpe et al. 2011, for more detailed explanation of coring techniques).

Shipboard delineation was attempted of lithostratigraphic surfaces observed in core that may correspond with seismic surfaces recognized by Lu and Fulthorpe (2004) (Fig. 2; Fulthorpe et al. 2011). One stepwise transition in lithofacies is associated with lithostratigraphic surface S13 (1853 m DSF), which is correlated with the Marshall Unconformity. Only lithostratigraphic surface S4 (~ 250 m) corresponds with a noticeable inflection point in the downhole lithofacies and physical-property datasets, which may reflect the association of this surface on the continental slope with a major sea-level lowstand between 0.44 and 0.91 Ma (Fulthorpe et al. 2011).

Porewater Geochemical Trends with Depth

Large and mostly gradual changes occur in the interstitial-water geochemistry with depth (Fig. 3). As noted earlier, interstitial-water measurements were limited by increasing lithification downhole, with the cores yielding progressively lower amounts of water with depth. Alkalinity increases from 2.4 mM at the seafloor to a maximum of 24.2 mM at 16.6 m, and then decreases to about 15 mM at 100 m and remains relatively constant down to about 400 m. From 400 to 600 m alkalinity declines steadily to about 2.3 and then remains in the range of 1.4–2.1 mM down to the base of sampling. The sulfate decline due to chemical reduction is almost exactly the inverse of the alkalinity increase, declining gradually over the 0–10 m interval, then abruptly from 10 to 24 m. Below 24 m, sulfate remains essentially at zero.

Both calcium and magnesium decrease over the depth interval when sulfate is reduced, then continue to decrease to minimum values (2 mM for Ca^{2+}, 10 mM for Mg^{2+}) in the depth range of 300–400 m (Fig. 3). Below 400 m both major cations increase to values of about 20–23 mM at depth of 600 m, where magnesium remains relatively constant to depths of about 1200 m. Calcium continues to increase to just above 30 mM in the deepest samples at 1386 m. The ratio of magnesium and calcium increases from 5 to > 9 from surface sediments to 18 m depth, then decreases to values around 2 at 500 m before gradually declining to 0.5 at 1300 m. Strontium concentrations start with seawater values around 0.1 mM and then increase slightly to values of 0.3 mM at a depth of 400 m before abruptly increasing further downhole to 2 mM at around 800 m. The concentrations then decrease to ~ 1.7 mM at maximum depth (Fig. 3).

Potassium decreases over the depth interval when sulfate is reduced, then increases to a maximum of about 10.5 mM at a depth of 150 m (Fig. 3). Potassium then declines to about 7 mM at 550 m, about 3 mM at 600 m, spikes back up to 5 mM at 650 m, before declining to about 2 mM in the deepest samples below 900 m. Iron concentrations, which show a trend similar to that of manganese (not shown), increase abruptly from seawater concentrations to a maximum of 34 μM at 26 m, decrease again to 4 μM at ~ 300 m, and finally increase to values ranging between 20 to 35 μM between 500 and 1386 m (Fig. 3). Lithium increases steadily from values of 25 μM at the sediment–water interface to ~ 50 μM at 450 m, then increases more abruptly to a maximum concentration of 166 μM at 700 m, before declining to ~ 100 μM at 800–900 m (Fig. 3). Below 900 m the lithium concentration increases again to 130 μM between 1000 and 1200 m, before dropping to 76 μM in the deepest sample.

SIGNIFICANCE AND APPLICATION

Diagenetic Trends with Depth

Eogenesis and the Transition to Mesogenesis

The zone of eogenesis occurs in the upper 50 m of the core, with a transitional lower interface downcore. We observe no evidence of compaction-induced features in this interval.

Eogenetic changes reflect the initial consolidation of sediments and are reflected primarily in porewater geochemical data from the upper 20 m of the sediment column. An interval of very gradual porewater sulfate depletion and alkalinity increase between 0 and 8.5 m depth (Fig. 3) represents either very slow organic-matter oxidation or a zone of present and past intense bioturbation. Very low levels of phosphate and the absence of ammonium in this interval are consistent with mixing by bioturbation. Sulfate, calcium, and magnesium decline from 8.5 to 16.6 m, whereas alkalinity (predominantly bicarbonate ions) increases through this interval. The amount of carbon oxidation during sulfate reduction is proportional to the alkalinity increase, with stoichiometry suggesting that two-thirds of the sulfate reduction is the result of organic-material oxidation, the other one-third, the result of methane oxidation (Fig. 6; Berner 1981; Fulthorpe et al. 2011; Arning et al. 2015).

The decreases in calcium and magnesium are likely related to authigenic carbonate precipitation. It is in this ~ 10 m region where carbonate-cemented nodules first occur (Fig. 4) in the section. As mentioned earlier, these are dominantly dolomite with $\delta^{13}C$ and $\delta^{18}O$ isotopic values of –20.4‰ VPDB and 6.7‰ VPDB respectively (details in Carson and Marsaglia 2015). $\delta^{13}C$ values below –5‰ VPDB and $\delta^{18}O$ isotopic values > 0‰ VPDB indicate a methane influence in authigenic carbonate precipitation (Naehr et al. 2007).

The interval between 50 m and ~ 300 m likely represents the transition from eogenesis to mesogenesis as recognized in alkalinity profiles. Alkalinity remains relatively constant down to about 50 m after an initial 2 mM alkalinity decrease beneath the sulphate-reduction zone, indicating that organic-matter oxidation is replenishing bicarbonate as rapidly as it is removed by methane generation and carbonate precipitation (Fig. 3). The gradual decline in alkalinity from about 14 mM to 1.5–2.5 mM between 100 and 350 m probably represents decreased microbiological activity resulting in the oxidation of organic matter, and the consequential microbially mediated reduction of dissolved CO_2 to produce methane. Rare carbonate (marlstone) nodules (Fig. 4) in this interval (e.g., ~ 155 m) are likely "fossil" cementation horizons similar to that observed in the uppermost cores, because alkalinity levels are too low to suggest supersaturated porewaters in this depth range.

With further burial these eogenetic features may be overprinted by mesogenetic phenomena. No fossil eogenetic nodule horizons were recognized on core split surfaces below 300 m, but may exist within cores. Furthermore, we note that whereas glauconite does not appear to be currently forming in the upper section at Site U1352, glauconite is present at depth in the core. Assuming that the glauconite-bearing intervals in Unit II are *in-situ* deposits, they were likely formed under past eogenetic conditions near the sediment–water interface on the slope (e.g., Worden and Morad 2009; Glenn and Arthur 1988). Alternatively, glauconite-filled bioclasts and glauconite clasts may have been

transported by bottom currents to the site from up-slope areas where the glauconite formed.

Mesogenesis

We delineate the zone of mesogenesis below 300 m based on the observations of porosity loss due to compaction, minor cementation, and minor mineral replacement. The main mesogenetic process we observe is porosity loss due to compaction.

Porosity loss due to compaction becomes prevalent in lithostratigraphic units IC and II and more pronounced below 1350 m. As described in the results section, porosity loss is recognized by compacted and fractured mollusk shells, distortion of clay-filled burrows, chemical compaction of foraminifer tests, and development of dark seams and stylolites (Figs. 4, 5). Differential compaction and dissolution also are recognized around darker laminae and burrow fills that are potentially associated with organic matter or higher clay content, which appears to enhance chemical compaction, creating darker seams and leading to the formation of stylolites (see Von Bergen and Carozzi 1990). The amount of organic matter, mostly < 1% TOC throughout the hole (Fulthorpe et al. 2011) declines down-section starting at ~ 1823 m (Sample U1352C-137R-2, 58–60 cm). It is noteworthy that more calcareous samples below this interval show evidence for chemical compaction only where there is minor organic matter (e.g., 1620 m).

Choquette and James (1987) draw a connection between pressure solution (chemical compaction), clay and silt content, and carbonate cementation. They noted that siliciclastic mud content affects the nature of pressure solution, ranging from serrated stylolites in more pure limestones to nonsutured seams and wispy seams in more "dirty" limestones. This is what we see at Site U1352, where well developed stylolites are present only near the base of the hole below 1600 m. These have been described in some detail by Vandeginste and John (2013). Below 1852 m (Unit III), the lithology is a foraminiferal micritic limestone with clay minerals concentrated in stylolites (offshore equivalent of the Amuri Limestone). The stylolites are best developed at the top of this interval, where they exhibit higher amplitudes, thicker clay seams, and distinct crosscutting relationships (Fig. 4). Because Unit III is so distinctively different from the younger Unit I and II lithologies in terms of lithology, color, and induration and because it is separated from those younger units by a fundamental unconformity, we cannot unequivocally relate our diagenetic observations with regard to Unit III to increasing burial depth alone.

Geochemical observations support the production of cements from reprecipitation of dissolved carbonate. The mesogenetic loss of porosity by cementation is indicated by primary intraparticle to interparticle carbonate and pyrite (e.g., Fig. 5A, B). Cementation is noted as both intraparticle (e.g., up to 20% as microcrystalline calcite filling foraminifer chambers; Subunit IIB, 1189–1693 m) and interparticle in better-sorted grainstone, siltstone, and sandstone laminae and burrow fills.

Porewater geochemistry is consistent with active cementation in this interval below 300 m. An alkalinity decrease and a calcium increase in the interval from 350 to 600 m corresponds to decreasing preservation of calcareous microfossils, as noted shipboard (Fulthorpe et al. 2011). Some exchange of magnesium for calcium in the dissolution and reprecipitation of carbonates during diagenesis is indicated by the greater declines in the Mg/Ca ratio and higher carbonate content (Fig. 3). Below 400 m, strontium, calcium, and

magnesium pore-water profiles are similar (Fig. 3). High strontium values (> 20 times seawater) can be explained by dissolution of Sr-rich aragonite in the sediments and recrystallization and cementation (Ando et al. 2006). Indeed, aragonitic mollusk fragments are present in the section and locally dissolved to form moldic pores (Carson and Marsaglia 2015).

Calcium remains at low levels (< 4 mM) in pore water until 400 m, and then increases to a steady value below 800 m (Figs. 2, 3). This is a common pore-fluid profile in sections dominated by carbonate sediment with little influence of any diffusive flux from below (McDuff and Gieskes 1976). This observation is consistent with the higher content of carbonate minerals in cores below about 600–700 m.

Isotopic analyses of three calcite-cemented sandstones and marlstones between 689 to 747 m yield normal marine signatures: $\delta^{13}C$ values of 0.55‰ to 0.62‰ and $\delta^{18}O$ values of –0.1‰ to 1.02‰ (all VPDB). One sample from ~ 700 m with higher Mg calcite had slightly higher (2.83‰ VPDB) carbon and oxygen (1.92‰ VPDB) values (details in Carson and Marsaglia 2015). High percentages of interparticle cement in at least one sample suggest that these carbonate cements from deeper in the section likely precipitated near the sediment surface as eogenetic features and here are buried, relict features. We note that Carson and Marsaglia (2015) selected these intervals for bulk isotopic analysis because they had minimal bioclastic carbonate; however, they exhibited varying amounts of micritic matrix to cement which might yield normal marine isotopic signatures.

There is also evidence for silica diagenesis at depth. Rapid increase and then decrease of lithium concentrations from 450 to 800 m are within a zone of high variance of porewater silica concentrations (Fulthorpe et al. 2011). Shipboard scientists (Fulthorpe et al. 2011) noted a pronounced decrease in siliceous microfossil content below 700 m, but minor authigenic quartz (chert) was not observed in thin sections until greater depth (1142 m). The transformation of biogenic opal to opal-A is likely to be a major source of lithium, but high lithium contents may also be related to clay-mineral diagenesis (e.g., Martin et al. 1991).

Comparison to Outcrop and Subsurface Studies of Diagenetic Trends with Depth

By and large, the changes in lithology described above are consistent with the broad nature of Neogene sedimentation in the New Zealand region, namely that fine-grained sediments predominated during the Neogene and that sediments were typically more calcareous in the early Miocene and Oligocene to late Eocene (King et al. 1999).

Comparable outcrop and subsurface studies addressing compaction and cementation processes without evidence of a meteoric influence and relating them to burial depth are limited, and perhaps surprisingly the few examples in the literature are “local” in South Australia and New Zealand. For example, Nicolaides and Wallace (1997) and Nicolaides (1995) studied compaction, pressure solution, and cementation in a similar-latitude Tertiary succession (the Clifton Formation) in southern Australia, which accumulated in a late Mesozoic extensional basin (Otway Basin). They inferred minimal uplift of the unit (~ 100 m) and assumed that the formation is currently at its maximum burial depth (~ 500–700 m). Porosities range from 40% at the top of the section to 10% at the base, similar to the range measured at Site U1352 (Fig. 2). In detail, Nicolaides and Wallace (1997) observed pressure solution at grain boundaries at depths of less than 160 m,

nonsutured dissolution seams at 190 m, and microstylolites at depths of 550 m and greater. They concluded that stylolitization requires burial depths of greater than 700 m, somewhat consistent with studies by Lind (1993) and Fabricius and Borre (2007), who found that incipient (flaser) stylolites formed below 470 m and well-developed stylolites below 830 m in a thick (1 km+) pelagic carbonate section on the Ontong Java Plateau. At Site U1352, pressure solution at grain boundaries starts at ~ 350 m but significant pressure solution does not occur until a depth of 1141 m, and the most developed "classic" stylolites occur at much greater depths in Unit III below 1800 m. Finally, Nelson et al. (1988) used oxygen stable-isotope analyses as a means of estimating cementation in the Oligocene Te Kuiti Group from the North Island, New Zealand, at burial depths of 400–1000 m, with according to Nicolaides and Wallace (1997) a "critical pressure-dissolution threshold at 500 m."

In sum, our data support inferences made from other outcrop studies regarding the depth of diagenetic transitions and the compositional influences on those transitions.

Potential Influence of Sediment Compositional on Diagenetic Trends

We note that there are no distinct compositional changes in mud components based on shipboard smear-slide analyses into the Mesogenetic zone at ~ 300 m at Site U1352 (Fulthorpe et al. 2011). However, this interval roughly corresponds to a broad change in clay content in the mud fraction as determined by XRD analyses (Fig. 2), as well as sand composition as determined by Bender-Whitaker (2013) and Bailey (2016). Bailey (2016) and Bender-Whitaker (2013) indicate that the deeper Pliocene–Oligocene section (281–1607 m) contains sand that is, on average, more enriched in quartz, metamorphic lithic grains, and mica. Although the sand and sandstone samples exhibit similar percentage ranges of sand-size bioclasts, as noted previously the overall carbonate content of the section increases with age and burial depth (Fig. 2). Therefore, we cannot completely rule out a sediment-composition effect on trends in compaction and diagenesis in the Site U1352 succession.

Origin and Significance of Glauconitic Injection Features

The compaction and diagenetic history of the succession at Site U1352 includes a phase of clastic injection. Injectites refer to the forcible intrusion of the injectite sediment (glauconitic sand in the Canterbury Basin case), as opposed to passively filled clastic dikes, and are generally explained by some combination of loading and/or fluid overpressuring in the sediment with a triggering mechanism (Beacom et al. 1999; Huuse et al. 2010).

The dark abrupt laminae of Subunit IIC (~ 1700–1770 m) are interpreted as injection features because they truncate some cemented foraminifers, indicating that they are later-stage post-cementation features. In some instances, the contacts between the limestone and the injectites have been overprinted by chemical compaction and stylolitization. However, the crosscutting relationships are distinct in areas of no apparent chemical compaction. Furthermore, clasts of host limestone can be seen floating in the glauconitic injectite (see also Fulthorpe et al. 2011).

Clastic sills and dikes have been described from many subsurface (e.g., Dixon et al. 1995; Jonk et al. 2005), and outcrop (e.g., Scott et al. 2009; Diggs and McBride 1990; Diggs 2007) settings, but the processes by which they are formed remain poorly constrained (Hurst et al. 2003; Huuse et al. 2010). Similar glauconitic sand injection

features have been described elsewhere in New Zealand, including in the Amuri Limestone facies, the onshore equivalent of Unit III at Site U1352 (Lewis et al. 1979; Browne 1987), and nearby onshore carbonates and volcanics at Oamaru (Lewis 1973; Lewis and Belliss 1984). Lewis et al. (1979) described broad (tens of meters wide) glauconite sandstones cutting the Amuri Limestone, with those sandstones sourced from an underlying Eocene formation. Browne (1987) described glauconitic sandstone in the Amuri Limestone occurring both as *in situ* turbidite sandstone beds in the Paleocene limestone, and as remobilized injectites that crosscut the stratigraphy. In the Oamaru example, remobilized Oligocene carbonate dikes crosscut shallow marine basaltic volcanic rocks (Lewis 1973). In comparison to the above, the Site U1352 injection features (Fig. 4) are better examples of small-scale, largely horizontal injection features.

Evidence for the source of the injected sand comes from the nearby Clipper-1 exploration well ~ 12 km to the WSW of Site U1352 (Fig. 1), which encountered 9 m of greensand (2281–2290 m), termed the Kokoamu Greensand, above the Amuri Limestone (our Unit IIC equivalent). This interval was not encountered at Site U1352 and may have been the source of the injected material.

The burial depth, timeframe, and cause of injectite formation can be somewhat constrained. Hurst et al. (2003) documented injection features that formed up to 500 m below the seafloor. Such dilational features have also been attributed to stress relaxation during the waning stages of stylolite formation (Sinha-Roy 2004). Petrographic evidence indicates that the injections occurred after formation of stylolites in the Amuri Limestone and cementation of the overlying units. The timescales needed to generate stylolites and how time is reflected in stylolite morphology have been debated (Koehn et al. 2007). There are few studies that provide direct evidence for the timing of stylolite generation. Fabricius and Borre (2007) documented progressive stylolitization of chalk on the Ontong Java Plateau. Their results suggest that at Site U1352, sediments must have been buried to at least 400–500 m before formation of the injection features. The answer may actually be in the upper part of the hole, in that formation of these features may require a mixture of harder cemented zones and overpressured unconsolidated sandy sediment. Cementation in calcareous mud and marl starts at 400 m at Site U1352, but the porosity and bulk-density data support a zone of less lithified and more lithified units starting at about 750 m. It is possible that the dilational phase-cementation in a stylolite in Sample U1352C-146R-3, 21–24 cm at ~ 1900 m may be related to an injection event, which must have occurred after significant burial. Carbonate injection features at nearby Oamaru (Lewis 1973) may be related to stresses due to differential loading or to volcanic doming or subsidence associated with localized magmatic processes active in the Eocene–Oligocene. Such a trigger mechanism could also be a causal factor for the injectites at Site U1352. Alternatively, the injections could be related to Alpine plate-boundary tectonics or rapid rates of sediment accumulation at the site.

Porosity–Depth Trends

Porosity–depth curves have been generated in numerous basins and tectonic settings, and by a range of methods, usually for end-member lithologies such as carbonates, sand (sandstone), and mud (shale). Decreases in porosity with depth revealed by such curves involves the effects of both compaction and cementation. For example, Schmoker and Halley (1982) found that porosity calculated from borehole electric logs exponentially

decreased in relatively pure carbonate intervals from Pleistocene to Cretaceous successions deposited in shallow-water environments on the Florida platform, starting at very high porosities at the near surface (up to ~ 55%) and decreasing to ~ 35–15% after 1–2 km of burial. Over half the initial porosity was lost by ~ 1.7 km of burial. Paxton et al. (2002) similarly found from petrographically determined intergranular porosity that for relatively uncemented quartz sandstones, a porosity reduction from about 42% for surficial sediments to about 28% at 1500 m burial depth was consistent for a large dataset of sandstones from many different types of sedimentary settings and ages. Another study by Halley and Schmoker (1983) emphasized the importance of cementation and pressure solution (chemical compaction) in porosity reduction, and pointed out the dearth of studies of this process in shallow-buried successions. They cited calculations by Neugebauer (1973, 1974) indicating that pressure solution should be significant in sediments exposed to low-Mg pore fluids with less than 1 km of burial, and linked pressure solution at shallow depths (~ 120 m) in some Florida limestones to fresh-water influence.

Porosity can be determined in a number of ways: from well logs, as visual porosity determined in impregnated thin sections, or from porosity measurements on samples. Well logs are available only for the upper portion of Site U1352, and the number of thin sections available is limited, so we have used porosity measurements on samples in the following discussion, as they provide multiple porosity values throughout the cored interval. Downhole discrete sample porosity data for Site U1352 are presented in Figures 7 and 8 together with representative modeled porosity–depth curves for various lithologies used in New Zealand basin analyses and from the literature. Our data show a wide scatter for a given depth but are broadly consistent with the modeled curves presented. Part of this scatter relates to the mixed lithologies encountered in the cores, from fine-grained siliciclastic mud(stone) to carbonate mud(stone) marl, to micrite and to interbedded sand(stone) (Figs. 7, 8). In addition, the measurements were made on samples from two different holes where different coring techniques were used. For Hole B, all cores were collected with APC (advanced piston core) and XCB (extended core barrel) drilling bits, while in the C hole, offset laterally by 20 m from Hole B, core was recovered using an RCB (rotary core barrel) bit. APC/XCB coring techniques will preferentially recover unlithified sediments and probably did not recover lithified intervals in the same abundance, whereas the RCB technique will preferentially recover more lithified lithologies over unlithified intervals. Consequently, the range in porosity for a given depth interval likely reflects the *in situ* distribution in values.

Despite this coring variability, the data show a consistent reduction in porosity from around 50% for surficial sediments to approximately 20% at 1500 m, to around 5–10% at the TD of 1927 m. As expected, these values are greater than those reported for sandstones by Paxton et al. (2002) but are similar to the carbonate data presented by Schmoker and Halley (1982) and to values for mixed siliciclastic–carbonate lithologies (such as Saito and Goldberg 1997). Our data show a wider range in porosity values beginning at about 500 m and a change in porosity values around 700–750 m at the Unit I–II boundary. The lower values likely relate to the different types of coring used between the two holes (U1352B and U1352C). The RCB cores captured more cemented, lower-porosity samples at equivalent depths sampled by the XCB cores in Hole B. Steps

(anomalous increases in porosity with depth) may exist between approximately 800 and 950 m, and again between 1600 and 1750 m, but we are uncertain how these could have formed. They may relate to some poorly understood sedimentary cyclicity and to the development of carbonate cements and stylolites, respectively, at those depths, though the latter would tend to reduce porosity (Fig. 7). The porosity–depth trend through the upper Hole B portion of the site are broadly consistent with the Manganui mudstone curve, which makes sense given the mud-dominated nature of this part of the succession (Fig. 7). The Manganui mudstone curve was developed from a series of wells in the Taranaki Basin, on the western side of New Zealand, that penetrated the Miocene Manganui Formation, a slope mudstone with subordinate sandstone, depositionally and lithologically similar to sediments at Site U1352. The lower portion of Site U1352 through the interval drilled by the Hole C again shows porosity–depth relationships very similar to the Manganui mudstone trend using the Schneider model and the two shale curves, but lower porosity than the two sandstone curves (Athey's Law and Schneider), the two micrite curves, and the Manganui mudstone curve using Athey's Law (see Schneider et al. 1996). This may be related to the loss of primary porosity via cementation.

Figure 8 shows lithology-specific data for the same sample set as described above, for samples that can be classified into silt(stone), clay(stone), sand(stone), and micrite (Fig. 8 A–D). As indicated above, some samples are mixtures of lithologies (e.g., subequal mixtures of silt and sand) and difficult to categorize and have been excluded. In Figure 8 we show only those samples with ≥ 50% silt, clay, sand, or micrite. By far the majority of data points are for silt(stone) (Fig. 8A), and they closely resemble the total sediment data presented in Figure 7 and the Manganui mudstone curve. Data points for clay(stone), sand(stone), and micrite (Fig. 8B–D) are limited but still show an overall downhole relationship similar to the total sediment data and the Manganui mudstone curve shown in Figure 7.

DISCUSSION

The processes by which porosity is lost during burial via compaction and cementation have traditionally been split between carbonate and siliciclastic lithologic end members, with carbonate studies avoiding intervals with significant terrigenous input and vice versa (e.g., Schmoker and Halley 1982). Outcrop and well-based studies have shown products of cementation and compaction products (e.g., fracturing of grains, chemical compaction, pressure solution at grain contacts, pore-fill cements) similar to those documented at Site U1352 in both carbonate (Bathurst 1974; Schmoker and Halley 1982; Halley and Schmoker 1983; Nelson et al. 1988; Moore 1989; Nicolaides 1995; Nicolaides and Wallace 1997; Fabricius and Borre 2007) and siliciclastic settings (Galloway 1984; Paxton et al. 2002). Many of these outcrop-based studies can only estimate the depths at which these diagenetic processes occurred.

For example, in their study of Oligocene limestone outcrops in North Island, New Zealand, Nelson et al. (1988) proposed that shallow-burial processes dominated to depths of 500–600 m with reduction in porosity through mechanical compaction and selective calcite cementation through dissolution and reprecipitation of skeletal material. They surmised that at depths between 600–1100 m porosity loss through pressure solution

(chemical compaction) continued with the development of microstylolitic solution seams, similar to what we observed at Site U1352.

In high-latitude, cool-water carbonate slope settings like those of New Zealand, components are dominantly calcitic and with low percentages of aragonitic components, whose diagenetic alteration promotes carbonate cementation (James 1997; Nicolaides 1995; Nelson et al. 2003). James (1997) suggests that in such cool-water sediments compaction and pressure solution (chemical compaction) may be more important in lithification than cementation. For this reason, Nelson et al. (2003) refers to New Zealand examples as having low "diagenetic potential," with cementation occurring only after deeper burial and pressure solution (chemical compaction) of calcitic bioclasts. This is what we have found to be the case in the Site U1352 sediments, with sparse cemented zones influenced by methane oxidation at shallow levels often showing aragonitic mollusk molds and finely crystalline burial cementation associated with an increasing degree of chemical compaction (pressure solution) at depth. The progressive lithification of sediments as documented in the petrographic and geochemical observations above proceeds by the interplay of cementation and both mechanical and chemical compaction.

Carbonate cementation is actively occurring at the site, incipient at very shallow depths (~ 10 m), and more pervasive in the interval 350 to 600 m, where it corresponds to a decrease in alkalinity and an increase in calcium and Sr in the porewater geochemistry. Petrographically these changes in pore-water chemistry are consistent with a decrease in calcareous fossils (principally foraminifers, especially milliolids) through this interval, via dissolution and chemical compaction. The progressive increase in Ca levels to a constant level at about 800 m suggests continued dissolution and cementation by carbonate and is consistent with the high carbonate-mineral content in cores below about 600–700 m.

Quartz too is observed to undergo downhole transformations, initially of biogenic opal to opal-A as reflected in the high Li content from 450 to 800 m. This transformation is likely to be a major source of lithium, although it may also be related to clay-mineral diagenesis. Minor authigenic quartz (chert) was not petrographically observed until a greater depth, in thin sections at 1142 m and then at several intervals below.

CONCLUSIONS

In this paper we describe a unique sedimentary record spanning a 1927-m-thick, Eocene to Recent fine-grained sedimentary succession. Core from this marine site, together with a range of downhole geochemistry logs, integrated with biostratigraphy, has allowed us to relate observed changes in petrography and diagenesis to these other downhole records, to provide an integrated documentation of how soft sediment changes with burial into an indurated rock.

Our study provides not only depth-constrained observations, but additionally, lithologic, petrophysical, and geochemical data to augment existing outcrop- and core-based diagenetic models. At Site U1352 we can demonstrate that carbonate cementation occurs from an early methane-oxidation-driven increase in alkalinity or to a later dissolution–reprecipitation–burial phenomenon. We document the progressive development of solution seams and stylolites over a wide depth range, with chemical compaction of carbonate components starting much earlier in the burial history (~ 350 m) than the depths (600–1100 m) previously suggested by Nelson et al. (1988).

The first direct evidence for compaction occurs at 347 m with the brittle fracturing of fossil fragments and interpenetration (brittle readjustment) of harder grains into softer milliolid foraminifer tests. Deeper in the hole, compaction is more pronounced. Evidence for compaction is present throughout Subunit IIC starting with grain fracturing, interpenetration, deformation of micrite-filled burrow margins, and, in places, the complete destruction of foraminifer tests. Pressure solution (chemical compaction) begins at 380 m and is common below 1440 m, with stylolite development below 1600 m, and sediment injection features below 1680 m. Taken together, our study illustrates the overarching role that pore-water geochemistry and carbonate-component mineralogy has in determining the interplay between cementation and both mechanical and chemical compaction.

ACKNOWLEDGMENTS

We thank the crew of the RV *JOIDES Resolution* for professional seamanship, excellent drilling, and the scientific support on board. GHB and SCG thank the Australia–New Zealand IODP Consortium (ANZIC), and KMM thanks the Consortium for Ocean Leadership U.S. Science Support Program for partly funding this work. Thanks also to funding agencies of the respective authors, and Mark Lawrence (GNS Science) and Cam Nelson (University of Waikato) for their thoughtful comments on an earlier draft. Karsten Kroeger (GNS Science) helped by providing compaction data for New Zealand basins, and Michelle Kominz (Western Michigan University) provided data on which Figure 8 was developed. Further improvements were the result of thoughtful detailed reviews by Gemma Barrie, Bill Heins, Stan Paxton, Associate Editor Joe Macquaker, and Editor Leslie Melim.

REFERENCES

Adams, J., 1980, Contemporary uplift and erosion of the Southern Alps, New Zealand: Geological Society of America, Bulletin, v. 91, p. 1–114.

Ando, A., Kawahata, H., and Kakegawa, T., 2006, Sr/Ca ratios as indicators of varying modes of pelagic carbonate diagenesis in the ooze, chalk and limestone realms: Sedimentary Geology, v. 191, p. 37–53.

Armenteros, I., 2010, Diagenesis of carbonates in continental settings, *in* Alonzo-Zarza, A.M., and Lawrence, H., eds., Carbonates in Continental Settings: Amsterdam, Elsevier, Developments in Sedimentology 62, p. 61–151.

Arning, E.T., Gaucher, E.C., van Berk, W., and Schulz, H.M., 2015, Hydrogeochemical models locating sulfate–methane transition zone in marine sediments overlying black shales: a new tool to locate biogenic methane?: Marine and Petroleum Geology, v. 59, p. 563–574.

Athey, L.F., 1930, Density, porosity, and compaction of sedimentary rocks: American Association of Petroleum Geologists, Bulletin, v. 14, p. 1–23.

Bailey, C., 2016, Provenance study of Miocene to Pliocene sand and sandstone intervals recovered on Expedition 317 in the Canterbury Basin, South Island, New Zealand [M.S. thesis]: California State University, Northridge, 69 p.

Bathurst, R.G.C., 1974, Marine diagenesis of shallow water calcium carbonate Sediments, *in* Donath, F.A., Stehli, F.G., and Wetherill, G.W., eds., Annual Review of Earth and Planetary Science, v. 2: Annual Reviews, p. 257–274.

Beacom, L.E., Anderson, T.B., and Holdsworth, R.E., 1999, Using basement-hosted clastic dykes as syb-rifting paleostress indicators: Geological Magazine, v. 136, p. 301–310.
Bender-Whitaker, C., 2013, Holocene–Pleistocene sand provenance in the Canterbury Basin, eastern South Island, New Zealand [M.S. thesis]: California State University, Northridge, 103 p.
Berner, R.A., 1981, A new geochemical classification of sedimentary environments: Journal of Sedimentary Petrology, v. 51 p. 359–365.
Browne, G.H., 1987, *In situ* and intrusive sandstone in Amuri facies limestone at Te Kaukau Point, southeast Waiararapa, New Zealand: New Zealand Journal of Geology and Geophysics, v. 30, p. 363–374.
Browne, G.H., and Field, B.D., 1985, The lithostratigraphy of Late Cretaceous to Early Pleistocene rocks of northern Canterbury, New Zealand: New Zealand Geological Survey, Record 6, 63 p.
Browne, G.H., and Naish, T.R., 2003, Facies development and sequence architecture of a late Quaternary fluvial–marine transition, Canterbury Plains and shelf, New Zealand: implications for forced regressive deposits: Sedimentary Geology, v. 158, p. 57–86.
Burley, S.D., and Worden, R.H., 2003, Sandstone diagenesis: recent and ancient: International Association of Sedimentologists, Reprint Series 4, 649 p.
Carson, D., and Marsaglia, K.M., 2015, Preliminary investigation of carbonate-cemented zones in IDOP cores from the Canterbury Basin, South Island, New Zealand: IODP Scientific Results, v. 317, http://publications.iodp.org/proceedings/317/204/204_.htm.
Carter, R.M., 1985, The mid-Oligocene Marshall Paraconformity, New Zealand: coincidence with global eustatic sea-level fall or rise?: Journal of Geology, v. 93, p. 359–371.
Carter, R.M., 2007, The role of intermediate-depth currents in continental shelf–slope accretion: Canterbury Drifts, SW Pacific Ocean, *in* Viana, A.R., and Rebesco, M., eds., Economic and Palaeooceanographic significance of contourite deposits: Geological Society of London, Special Publication 276, p. 129–154.
Carter, R.M., and Gammon, P., 2004, New Zealand maritime glaciation: millennial-scale southern climate change since 3.9 Ma: Science, v. 304, p. 1659–1662.
Carter, R.M., and Landis, C.A., 1972, Correlative Oligocene unconformities in southern Australasia: Nature Physical Science, v. 237, p. 12–13.
Carter, R.M., and Landis, C.A., 1982, Appendix: Oligocene unconformities in the South Island: Royal Society of New Zealand, Journal, v. 19, p. 42–46.
Carter, R.M., and Norris, R.J., 1976, Cainozoic history of southern New Zealand: an accord between geological observations and plate tectonic predictions: Earth and Planetary Science Letters, v. 31, p. 85–94.
Choquette, P.W., and James, N.P., 1987, Diagenesis 12. Diagenesis in Limestones 3: the Deep Burial Environment: Geoscience Canada, v. 1, p. 3–35.
Diggs, T.N., 2007, An outcrop study of clastic injection structures in the Carboniferous Tesnus Formation, marathon Basin, Trans-Pecos Texas, *in* Hurst, A., and Cartwright, J., eds., Sand Injectites: Implications for Hydrocarbon Exploration: American Association of Petroleum Geologists, Memoir 87, p. 209–219.

Diggs, T.N., and McBride, E.F., 1990, Concordant, discordant, and transitional clastic injection structures in the Tesnus Formation, Marathon Basin, Trans-Pecos Texas, *in* Laroche., T.M., and Higgins, L., eds., Marathon Thrust Belt, Structure, Stratigraphy and Hydrocarbon Potential: West Texas Geological Society and SEPM, Permian Basin Section, Field Seminar, p. 99–110.
Dixon, R.J., Schofield, K., Anderton, R., Reynolds, A.D., Alexander, R.W.S., Williams, M.C., and Davies, K.G., 1995, Sandstone diapirism and clastic intrusion in the Tertiary submarine fans of the Bruce Beryl Embayment, Quadrant 9, UKCS, *in* Hartley, A.J., and Prosser, D.J., eds., Characterisation of Deep-Marine Clastic Systems: Geological Society of London, Special Publication 94, p. 77–94.
Fabricius, I.L., and Borre, M.K., 2007, Stylolites, porosity, depositional texture, and silicates in chalk facies sediments: Ontong Java Plateau, Gorm and Tyra fields, North Sea: Sedimentology, v. 54, p. 183–205.
Field, B.D., and Browne G.H., 1989, Cretaceous and Cenozoic sedimentary basins and geological evolution of the Canterbury region, South Island, New Zealand: New Zealand Geological Survey, Bulletin 2, 94 p.
Findlay, R.H., 1980, The Marshall Paraconformity (Note): New Zealand Journal of Geology and Geophysics, v. 23, p. 125–133.
Fulthorpe, C.S., and Carter, R.M., 1991, Continental-shelf progradation by sediment-drift accretion: Geological Society of America, Bulletin, v. 103, p. 300–309.
Fulthorpe, C.S., Hoyanagi, K., Blum, P., and the Expedition 317 Scientists, 2011, Site U1352: Proceedings of the Integrated Ocean Drilling Program, v. 317, doi:10.2204/iodp.proc.317.104.2011.
Galloway, W.E., 1984, Hydrogeologic regimes of sandstone diagenesis, *in* McDonald, D.A., and Surdam, R.C., eds., Clastic Diagenesis: American Association of Petroleum Geologists, Memoir 37, p. 3–13.
Gieskes, J.M., Gamo, T., and Brumsack, H., 1991, Chemical methods for interstitial water analysis aboard *JOIDES Resolution*: Ocean Drilling Program, Technical Note 15, doi:10.2973/odp.tn.15.1991.
Glenn, C.R., and Arthur, M.A., 1988, Petrology and major element geochemistry of Peru margin phosphorates and associated diagenetic minerals: authigenesis in modern organic-rich sediments: Marine Geology, v. 80, p. 231–267.
Halley, R.B., and Schmoker, J.W., 1983, High-porosity Cenozoic carbonate rocks of South Florida: progressive loss of porosity with depth: American Association of Petroleum Geologists, Bulletin, v. 67, p. 191–200.
Hurst, A., Cartwright, J., and Duranti, D., 2003, Fluidization structures produced by upward injection of sand through a sealing lithology, *in* van Rendsbergen, P., Hills, R.R., Maltman, A.J., and Morley, C.K., eds., Subsurface Sediment Mobilization: Geological Society of London, Special Publication 216, p. 123–138.
Huuse, M., Jackson, C.A.-L., Van Rensbergen, P., Davies, R.J., Flemings, P.B., and Dixon, R.J., 2010, Evidence for fluid flow and subsurface sediment transport: prior to cementation of glauconitic sand. Subsurface sediment remobilization and flow in sedimentary basins: an overview: Basin Research, v. 22, p. 342–360.
James, N.P., 1997, The cool-water carbonate depositional realm, *in* James, N.P., and Clarke, J.A.D., eds., Cool-Water Carbonates: SEPM, Special Publication 56, p. 1–20.

Jonk, R., Hurst, A., Duranti, D., Parnell, J., Mazzini, A., and Fallick, A.E., 2005, Origin and timing of sand injection, petroleum migration, and diagenesis in Tertiary reservoirs, south Viking Graben, North Sea: American Association of Petroleum Geologists, Bulletin, v. 89, p. 329–357.
King, P.R., Naish, T.R., Browne, G.H., Field, B.D., and Edbrooke, S.W., 1999, Cretaceous to Recent sedimentary patterns in New Zealand: GNS Science, Folio Series 1, 35 p.
Koehn, D., Renard, F., Toussaint, R., and Passchier, C.W., 2007, Growth of stylolite teeth patterns depending on normal stress and finite compaction: Earth and Planetary Science Letters, v. 257, p. 582–595.
Lever, H., 2007, Review of unconformities in the late Eocene to early Miocene successions of the South Island, New Zealand: ages, correlations, and causes: New Zealand Journal of Geology and Geophysics, v. 50, p. 245–261.
Lewis, D.W., 1973, Polyphase limestone dikes in the Oamaru region, New Zealand: Journal of Sedimentary Petrology, v. 43, p. 1031–1045.
Lewis, D.W., and Belliss, S.E., 1984, Mid Tertiary unconformities in the Waitaki Subdivision, North Otago: Royal Society of New Zealand, Journal, v. 14, p. 251–276.
Lewis, D.W., Smale, D., and van der Lingen, G.J., 1979, A sandstone diaper cutting the Amuri Limestone, North Canterbury, New Zealand: New Zealand Journal of Geology and Geophysics, v. 22, p. 295–305.
Lind, I.L., 1993, Stylolites in chalk from Leg 130, Ontong Java Plateau: Proceedings of the Ocean Drilling Program, Scientific Results, v. 130, p. 445–451.
Lu, H., and Fulthorpe, C.S., 2004, Controls on sequence stratigraphy of a middle Miocene–Holocene, current-swept, passive margin: offshore Canterbury Basin, New Zealand: Geological Society of America, Bulletin, v. 116, p. 1345–1366.
Lu, H., Fulthorpe, C.S., and Mann, P., 2003, Three-dimensional architecture of shelf-building sediment drifts in the offshore Canterbury Basin, New Zealand: Marine Geology, v. 193, p. 19–47.
Martin, J.B., Kastner, M., and Elderfield, H., 1991, Lithium: sources in pore fluids of Peru slope sediments and implications for oceanic fluxes: Marine Geology, v. 102, p. 281–292.
McDuff, R.E., and Gieskes, J.M., 1976, Calcium and magnesium profiles in DSDP interstitial waters: diffusion or reaction?: Earth Planetary Science Letters, v. 33, p. 1–10.
Moore, C.H., 1989, Carbonate Diagenesis and Porosity: Amsterdam, Elsevier Science, Developments in Sedimentology 46, 338 p.
Morse, J.W., and Mackenzie, F.T., 1990, Geochemistry of Sedimentary Carbonates: Amsterdam, Elsevier Science, Developments in Sedimentology 48, 696 p.
Murray, R.W., Miller, D.J., and Kryc, K.A., 2000, Analysis of major and trace elements in rocks, sediments, and interstitial waters by inductively coupled plasma–atomic emission spectrometry (ICP-AES): Ocean Drilling Program, Technical Note 29, doi:10.2973/odp.tn.29.2000.
Naehr, T.H., Eichhubl, P., Orphan, V.J., Hovland, M., Paull, C.K., Ussler, W., III, Lorenson, T.D., and Greene, H.G., 2007, Authigenic carbonate formation at hydrocarbon seeps in continental margin sediments, a comparative study: Deep Sea Research, Part II: Topical Studies in Oceanography, v. 54, p. 1268–1291.

Nelson, C.S., Harris, G.J., and Young, H.R., 1988, Burial-dominated cementation in non-tropical carbonates of the Oligocene Te Kuiti Group, New Zealand: Sedimentary Geology, v. 60, p. 233–250.
Nelson, C.S., Winefield, P.R., Hood, S.D., Caron, V., Pallentin, A., and Kamp, P.J.J., 2003, Pliocene Te Aute limestones, New Zealand: expanding concepts for cool-water shelf carbonates: New Zealand Journal of Geology and Geophysics, v. 46, p. 407–424.
Neugebauer, J., 1973, The diagenetic problem of chalk: the role of pressure solution and pore fluid: Neues Jahrbuch für Geologie und Päleontologie, Abhandlungen, v. 143, p. 223–245.
Neugebauer, J., 1974, Some aspects of cementation in chalk, *in* Hsu, K.J., and Jenkyns, H.C., eds., Pelagic Sediments on Land and Under the Sea: International Association of Sedimentologists, Special Publication 1, p. 149–176.
Nicolaides, S., 1995, Cementation in Oligo-Miocene non-tropical shelf limestones, Otway Basin, Australia: Sedimentary Geology, v. 95, p. 97–121.
Nicolaides, S., and Wallace, M.W., 1997, Pressure-dissolution and cementation in an Oligo-Miocene nontropical limestone (Clifton Formation) Otway Basin, Australia, *in* James, N.P., and Clarke, J.A.D., eds., Cool-Water Carbonates: SEPM, Special Publication 56, p. 249–261.
Paxton, S.T., Szabo, J.O., Ajdukiewicz, J.M., and Klimentidis, R.E., 2002, Construction of an intergranular volume compaction curve for evaluating and predicting compaction and porosity loss in rigid-grain sandstone reservoirs: American Association of Petroleum Geologists, Bulletin, v. 86, p. 2047–2067.
Saito, S., and Goldberg, D., 1997, Evolution of tectonic compaction in the Barbados accretionary prism: estimates from logging-while-drilling: Earth and Planetary Science Letters, v. 148, p. 423–432.
Schmoker, J.W., and Halley, R.B., 1982, Carbonate porosity versus depth: a predictable relation for South Florida: American Association of Petroleum Geologists, Bulletin, v. 66, p. 2561–2570.
Schneider, F., Potdevin, J.L., Wolf, S., and Faille, I., 1996, Mechanical and chemical compaction model for sedimentary basin simulators: Tectonophysics, v. 263, p. 307–313.
Scott, A., Vigorito, M., and Hurst, A., 2009, The process of sand injection: internal structures and relationships with host strata (Yellowbank Creek injectite complex, California, U.S.A.): Journal of Sedimentary Research, v. 79, p. 568–583.
Shinn, E.A., Halley, R.B., Hudson, J.H., and Lidz, B.H., 1977, Limestone compaction: an enigma: Geology, v. 5, p. 21–24.
Sinha-Roy, S., 2004, Antitaxial fibrous bands in differentiated stylolites: Geological Society of India, Journal, v. 63, p. 387–405.
Shipboard Scientific Party, 2004, Explanatory notes, *in* Tucholke, B.E., Sibuet, J.-C., Klaus, A., et al., eds., Proceedings of Ocean Drilling Project, Initial Reports 210: College Station, Texas, Ocean Drilling Program, p. 1–69.
Stone, W.N., and Siever, R., 1996, Quantifying compaction, pressure solution, and quartz cementation in moderately- and deeply-buried quartzose sandstones from the Greater Green River Basin, Wyoming, *in* Crossey, L.J., Loucks, R., and Totten, M.W., eds., Diagenesis and Fluid Flow: Concepts and Applications: SEPM, Special Publication 55, p. 129–150.

Sutherland, R., Davey, F., and Beavan, J., 2000, Plate boundary deformation in South Island, New Zealand, is related to inherited lithospheric structure: Earth and Planetary Science Letters, v. 177, p. 141–151.
Sutton, P.J.H., 2003, The Southland Current: a subantarctic current: New Zealand Journal of Marine and Freshwater Research, v. 37, p. 645–652.
Tippett, J.M., and Kamp, P.J.J., 1993, Fission track analysis of the late Cenozoic vertical kinematics of continental Pacific crust, South Island, New Zealand: Journal of Geophysical Research, v. 98, p. 16,119–16,148.
Vandeginste, V., and John, C.M., 2013, Diagenetic implications of stylolitization in pelagic carbonates, Canterbury Basin, New Zealand: Journal of Sedimentary Research, v. 83, p. 226–240.
Villasenor, T., Jaeger, J.M., Marsaglia, K.M., and Browne, G.H., 2015, Evaluation of the relative roles of global versus local sedimentary controls on middle to Late Pleistocene formation of continental margin strata, Canterbury Basin, New Zealand: Sedimentology, v. 62, p. 1118–1148.
Von Bergen, D., and Carozzi, A.V., 1990, Experimentally-simulated stylolitic porosity in carbonate rocks: Journal of Petroleum Geology, v. 13, p. 179–192.
Wellman, H.W., 1979, An uplift map for the South Island of New Zealand, and a model for uplift of the Southern Alps, *in* Walcott, R.I., and Cresswell, M.M., eds., The Origin of the Southern Alps: Royal Society of New Zealand, Bulletin, v. 18, p. 13–20.
Worden, R.H., and Morad, S., 2009, Clay Minerals in Sandstones: Controls on Formation, Distribution and Evolution: Oxford, U.K., Blackwell, Publishing, DOI: 10.1002/9781444304336.ch1.
Received 25 October 2015; accepted 10 January 2017.
FIGURE CAPTIONS
FIG. 1.—**A)** Map of the New Zealand region showing the location of Site U1352 and the other sites (U1351, U1353, and U1354) drilled during Expedition 317, the Clipper and Resolution-1 wells, bathymetry and extent of drift units. **B)** Seismic section across Site U1352. **C)** Interpretation of seismic section in Part B. The numbering of drifts in Part A is after Lu et al. (2003). The numbered intervals (4 to 19) in Part C are seismic sequence boundaries (after Lu and Fulthorpe 2004), and MP at the base of the figure is the Marshall Paraconformity. The four Site U1352 drill holes are displaced slightly from each other, and all are located within the black dot in this figure. Figures are slightly modified from Fulthorpe et al. (2011).
FIG. 2.—Downhole variation in age, lithostratigraphy (units/subunits), core recovery (black is recovered core), lithology (see below), grain size, thin-sectioned intervals and petrographic observations, physical properties (natural gamma, porosity, bulk density), and mineral (carbonate, quartz, and clay) content for Site U1352. Circled numbers relate to the major lithologies present (colored patterns) as follows: (1) chalk to limestone, (2) marlstone to sandy marlstone, (3) muddy sandstone, (4) mudstone, (5) sandy mudstone, (6) interbedded silt(stone) and mud(stone), and (7) interbedded sand(stone) and mud(stone). Natural-gamma radiation was measured directly from core (counts per second), porosity and bulk density were determined by measurement of wet mass, dry mass, and dry volume, calcite weight% is from coulometry analyses, and content of quartz and total clay are from shipboard XRD analyses. Data from the two deepest holes,

Hole B and Hole C (ship shifted 20 m horizontally between holes), are combined for the purposes of the figure. The lighter-color symbols and lines on plots are for Hole B, the darker ones for Hole C; the switch from Hole B to Hole C is marked in the stratigraphic column. See Fulthorpe et al. (2011) for details. Data can be found at //http://publications.iodp.org/proceedings/317/317toc.htm#Supplementary_material.

FIG. 3.—Downhole variation of interstitial water, alkalinity, geochemical parameters, and methane from headspace analysis relative to lithostratigraphy in Holes U1352A (red symbols), U1352B (black symbols), and U1352C (blue symbols). Lithostratigraphic units I to III are indicated. Parameters are yield of interstitial water (IW) per cm of squeezed whole-round cores, alkalinity (mM), magnesium (mM), calcium (mM), strontium (mM), potassium (mM), iron (μM), lithium (μM), methane (ppmv), ammonium (mM), sulfate (mM), and phosphate (μM). IAPSO seawater values are shown with the black filled triangle and marked with "SW." All data are from Fulthorpe et al. (2011).

FIG. 4.—Photographs of representative core intervals down through Units I, II, and III at Site U1352, emphasizing the nature and occurrence of lithified intervals, which range from sparse and thin to pervasive with increasing depth of burial. Cores with H (piston) and X (extended core barrel) identifiers are from Hole U1352B, and those with R (rotary) identifiers are from Hole U1352C. Core section is given by dashed number and interval in section indicated in centimeter scale on left of image. Image 2H-2 is a hard nodule in a burrowed gray mudstone and dark gray very fine sand. Image 17H-4 shows hard, fragmented nodule in gray mud. Image 42X-5 shows indurated olive very fine sandy mudstone with scattered shell fragments in drilling-disturbed mudstone. Image in 65X-1 shows fragmented marlstone. Image in 56R-1 shows core fragments consisting of greenish-gray sandy marlstone. Image of 104R-7 shows intact core segment of greenish-gray sandy marlstone. Image in 112R-2 shows greenish-gray sandy marlstone with vague (burrowed?) wavy to planar bedding. Image in 123-R-2 shows intact core segments with gray, slightly glauconitic, sandy marlstone with discrete burrows and pronounced wavy lamination. Image 136R-4 consists of light-gray planar-laminated slightly glauconitic sandy limestone core with very dark greenish-gray, well sorted, very fine to fine glauconitic sandstone (injectite) that crosscuts laminated fabric in lighter sandy limestone. Image in 141R-2 consists of white burrowed limestone core fragments crosscut by dark, serrated stylolites.

FIG. 5.—Photomicrographs of samples from Hole U1352C with 100 micron scale bars. **A)** Sample from core 85R, section 1, 140 cm (~ 1348 m) showing remnants (m) of a milliolid foraminifer (characteristic reddish brown test) highly deformed by mechanical compaction and pressure solution (chemical compaction). Note presence of pyrite (opaque) and carbonate (clear) cement in planktonic foraminifer. **B)** Same view as Part A but with polars crossed. **C)** Sample from core 61R, section 1, 21 cm (~ 1190 m) showing common pressure solution (chemical compaction) of carbonate foraminifers at grain contacts marked by "v"s. **D)** Sample from core 95R, section 6, 39 cm (~ 1439 m) with polars crossed, showing fractured echinoid fragment (e) in concavo-convex contact (marked by "v"s) with quartz and feldspar. **E)** Sample from core 105R, section 2, 77 cm (~ 1528 m) showing dissolution of foraminifer along bedding-parallel dark seams ("s"s). **F)** Same view as in Part E but with polars crossed showing truncation of birefringent foraminifer test. **G)** Sample from core 135R, section 5, 38 cm (~ 1809 m) showing

pressure solution (chemical compaction) of foraminifer (F) along contacts ("v"s) with round, green pelletal glauconite (plane light). **H)** Sample from core 146R, section 3, 24 cm (~ 1902 m) showing dissolution truncation of foraminifers ("v"s) along stylolite in micritic limestone (polars crossed).

FIG. 6.—Plot showing stoichiometry of the sulfate-reduction zone for the 12 samples shallower than 17 m in Hole U1352A. Equations for methane oxidation (bottom) and organic-matter oxidation (top) are shown. Data from Hole U1352A plot close to the 1.5:1 line (correlation line and equation are shown in red). Plot is taken from Fulthorpe et al. (2011).

FIG. 7.—Porosity–depth curve from Site U1352 based on measured porosity from samples collected in the B (upper portion of diagram) and C (lower portion of diagram) hole. The B and C holes used different coring techniques (APC/XCB in Core B and RCB in Core C, as explained in the text), giving potentially different porosity measurements. For reference, other compaction curves are presented. Manganui mudstone curves come from the Miocene Manganui Formation in the Taranaki Basin, New Zealand, derived from Athey's Law (after Athey 1930) and the Schneider model (after Schneider et al. 1996). Curves are also presented for shale, micrite, and sandstone lithologies, and all are based on basin model datasets developed by GNS Science (K. Kroeger, GNS Science, personal communication 2015).

FIG. 8.—Porosity-depth curves from Site U1352, showing porosity values for **A)** silt(stone), **B)** clay(stone), **C)** sand(stone), and **D)** micrite lithologies, and the same modeled compaction curves as shown in Figure 7.

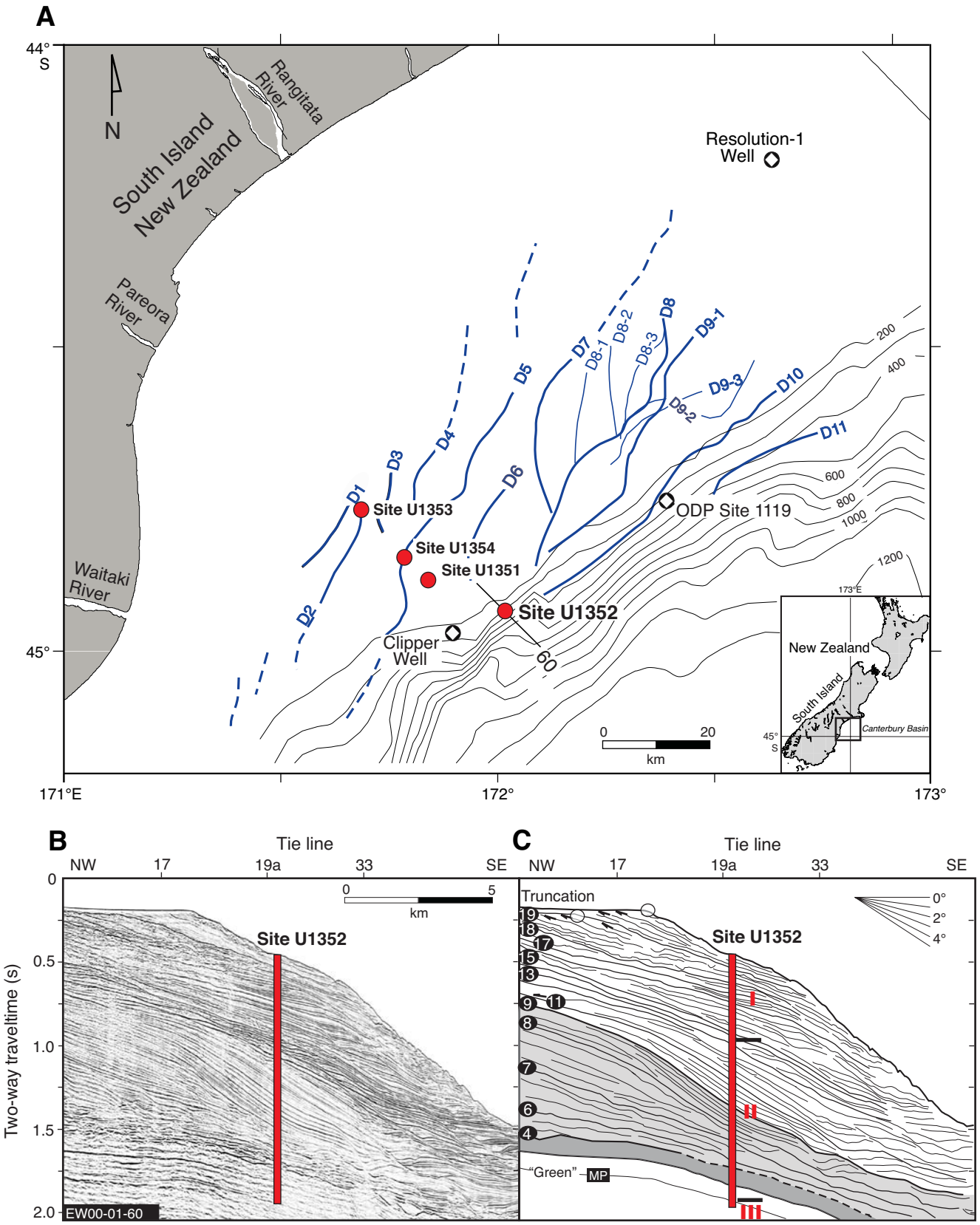
A
44° S
N
South Island
New Zealand
Rangitata River
Pareora River
Waitaki River
Resolution-1 Well
D1
D2
D3
D4
D5
D6
D7
D8-1
D8-2
D8-3
D8
D9-1
D9-2
D9-3
D10
D11
Site U1353
Site U1354
Site U1351
Site U1352
Clipper Well
ODP Site 1119
200
400
600
800
1000
1200
60
0
20
km
173°E
New Zealand
South Island
Canterbury Basin
45° S
171°E
172°
173°
B
Tie line
NW
17
19a
33
SE
0
5
km
Site U1352
Two-way traveltime (s)
0
0.5
1.0
1.5
2.0
EW00-01-60
C
Tie line
NW
17
19a
33
SE
Truncation
0°
2°
4°
19
18
17
15
13
9
11
8
7
6
4
Site U1352
I
II
III
"Green"
MP

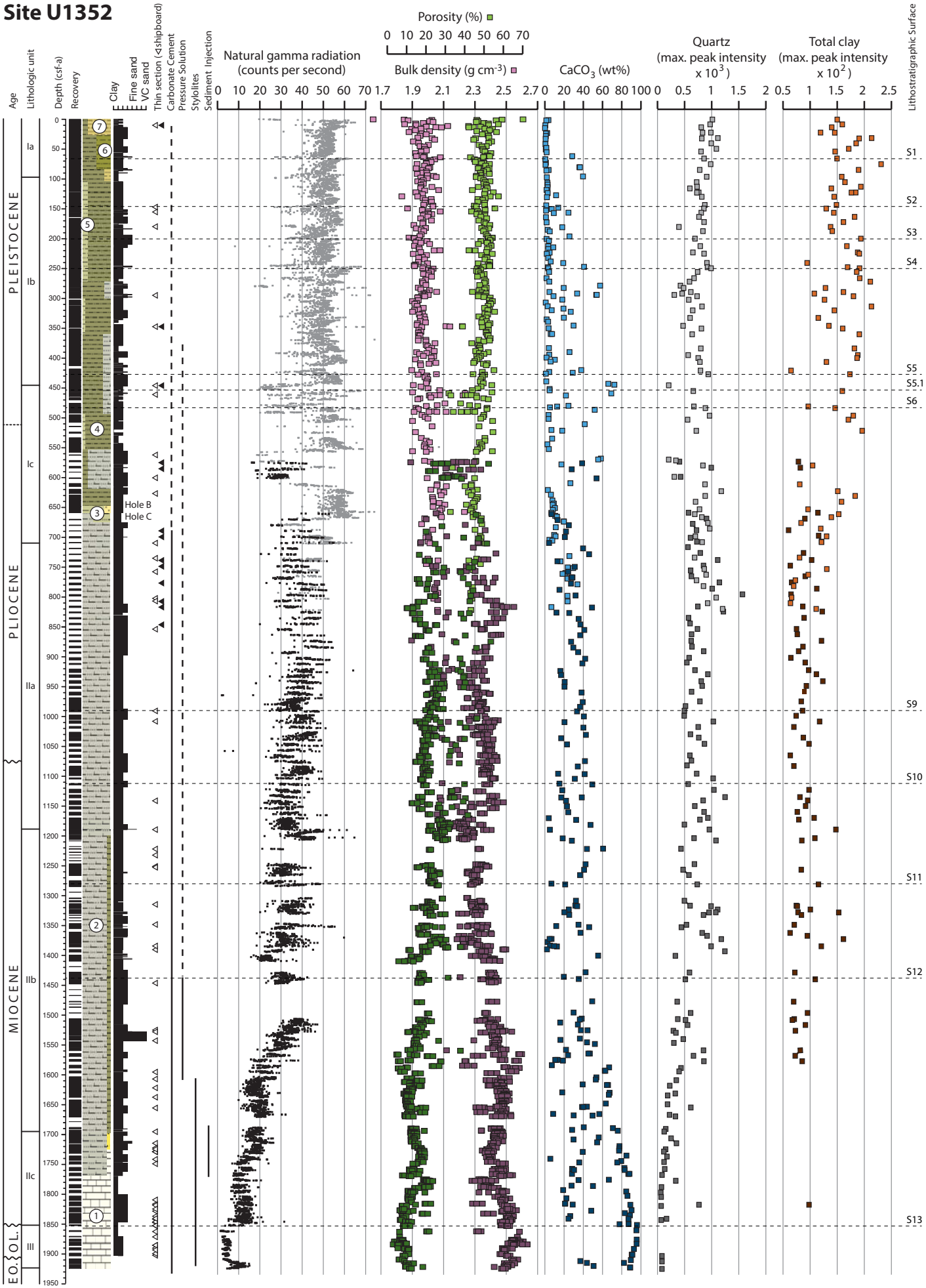
Site U1352
Age
Lithologic unit
Depth (csf-a)
Recovery
Clay
Fine sand
VC sand
Thin section (<shipboard)
Carbonate Cement
Pressure Solution
Stylolites
Sediment Injection
Natural gamma radiation (counts per second)
Porosity (%)
Bulk density (g cm-3)
CaCO3 (wt%)
Quartz (max. peak intensity x 10^3)
Total clay (max. peak intensity x 10^2)
Lithostratigraphic Surface
PLEISTOCENE
PLIOCENE
MIOCENE
EO.
OL.
Ia
Ib
Ic
IIa
IIb
IIc
III
Hole B
Hole C
S1
S2
S3
S4
S5
S5.1
S6
S9
S10
S11
S12
S13

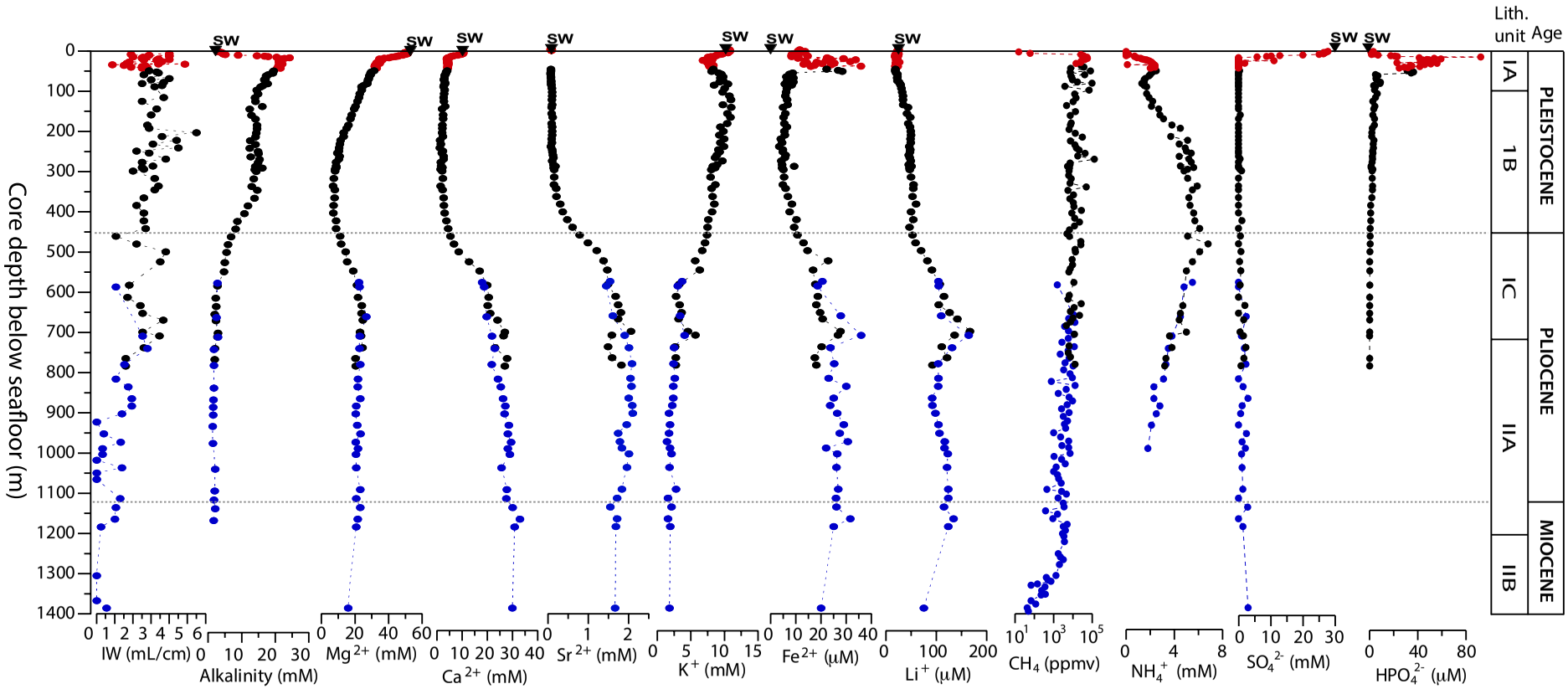
Core depth below seafloor (m)
0
100
200
300
400
500
600
700
800
900
1000
1100
1200
1300
1400
SW
IW (mL/cm)
0 1 2 3 4 5 6
Alkalinity (mM)
0 10 20 30
Mg2+ (mM)
0 20 40 60
Ca2+ (mM)
0 10 20 30 40
Sr2+ (mM)
0 1 2
K+ (mM)
0 5 10 15
Fe2+ (µM)
0 10 20 30 40
Li+ (µM)
0 100 200
CH4 (ppmv)
10^1 10^3 10^5
NH4+ (mM)
0 4 8
SO4 2- (mM)
0 10 20 30
HPO4 2- (µM)
0 40 80
Lith. unit
Age
IA
1B
IC
IIA
IIB
PLEISTOCENE
PLIOCENE
MIOCENE

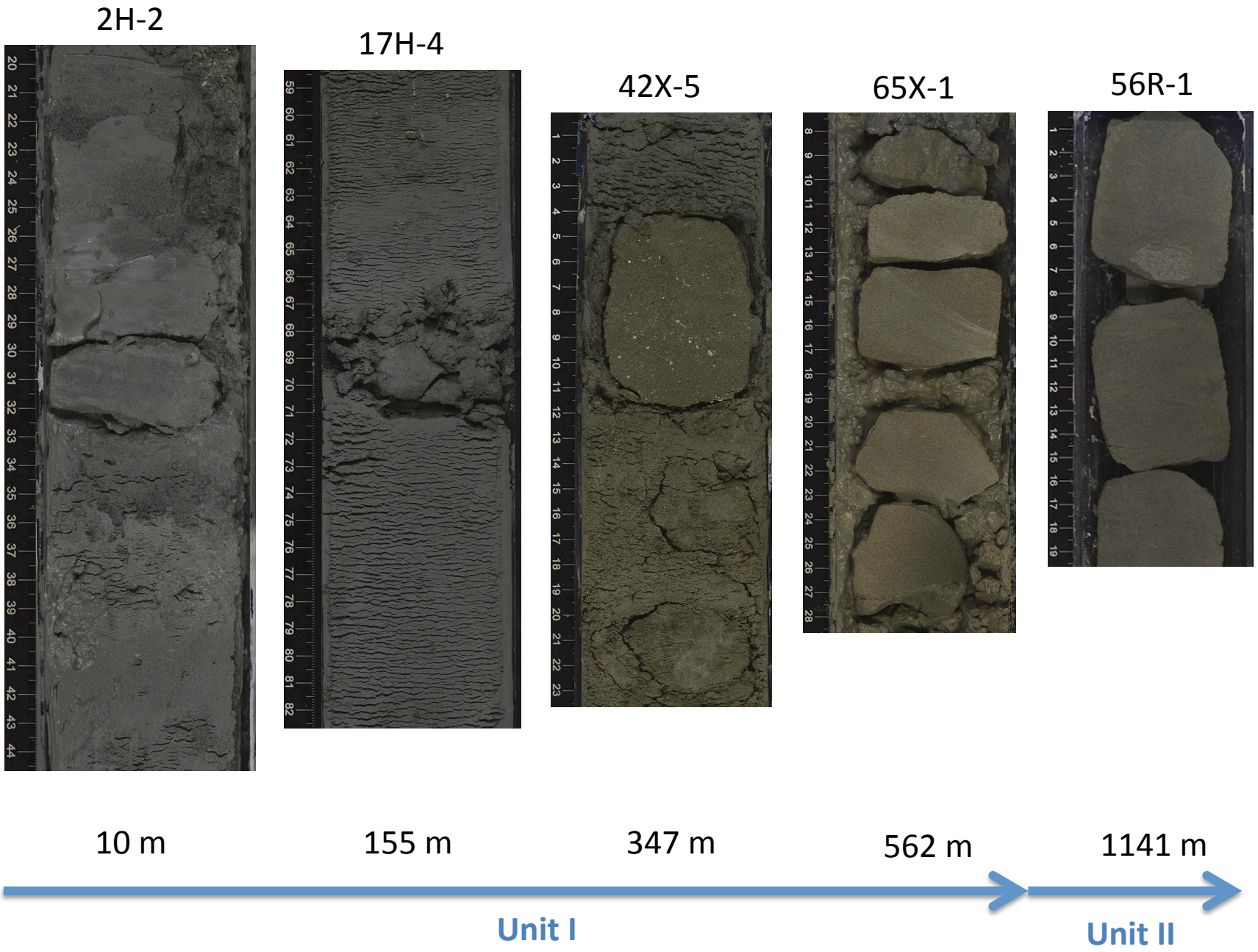
2H-2
17H-4
42X-5
65X-1
56R-1
10 m
155 m
347 m
562 m
1141 m
Unit I
Unit II

Figure 4

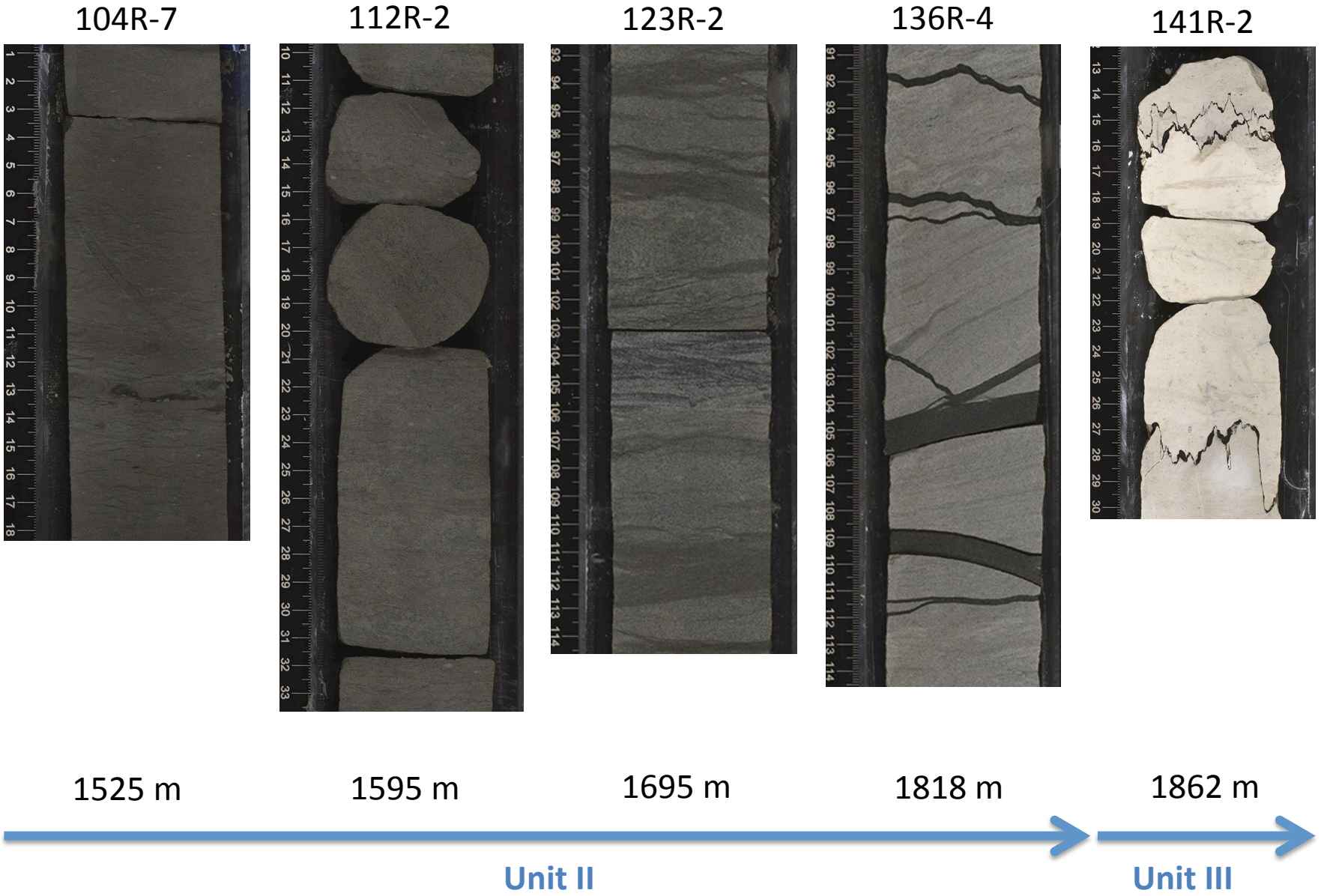

Figure 4 (Continued)

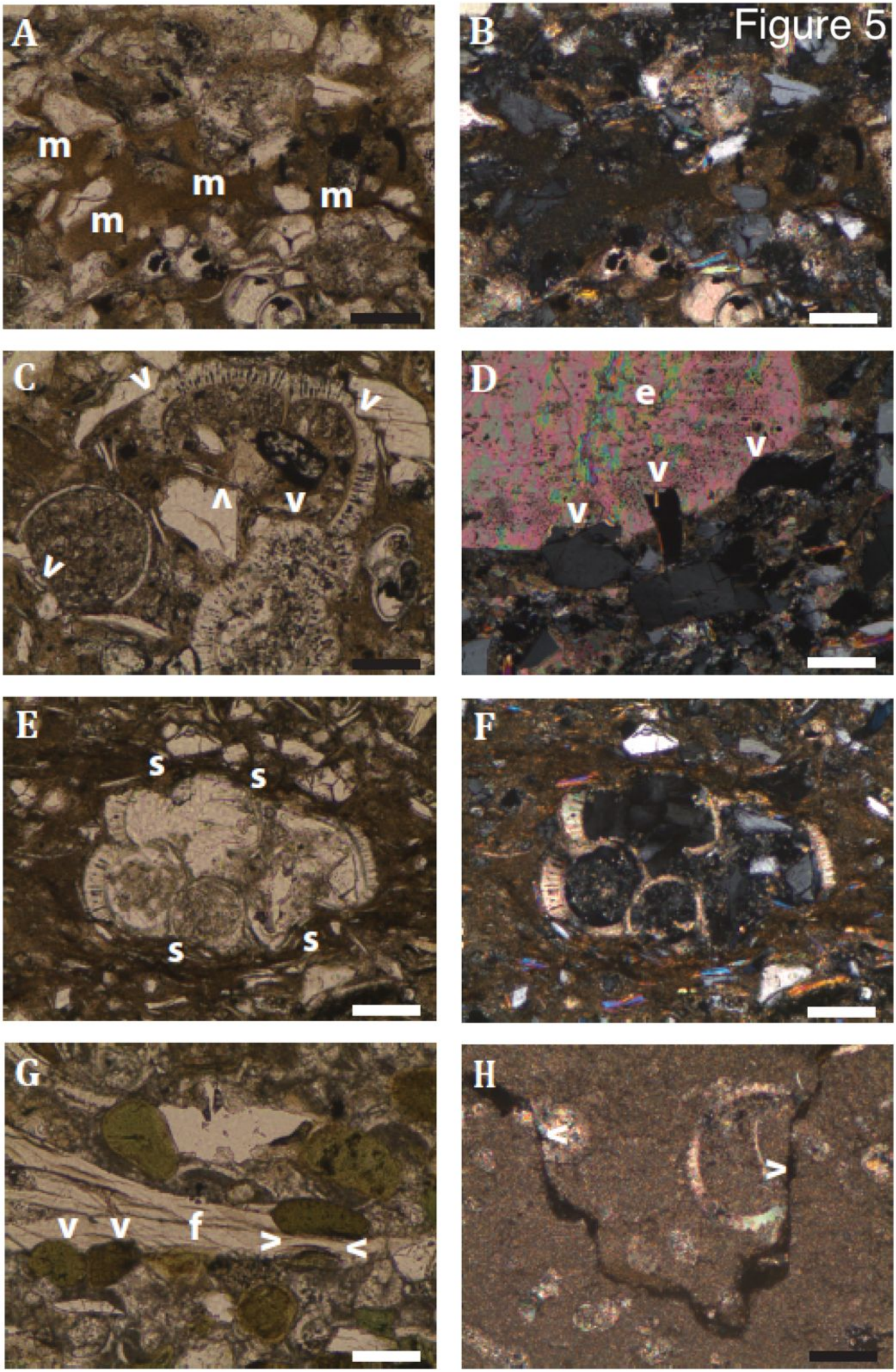
A
m
m
m
m
B
Figure 5
C
v
v
v
v
D
e
v
v
v
E
s
s
s
s
F
G
v
v
f
>
<
H
<
v

Figure 6

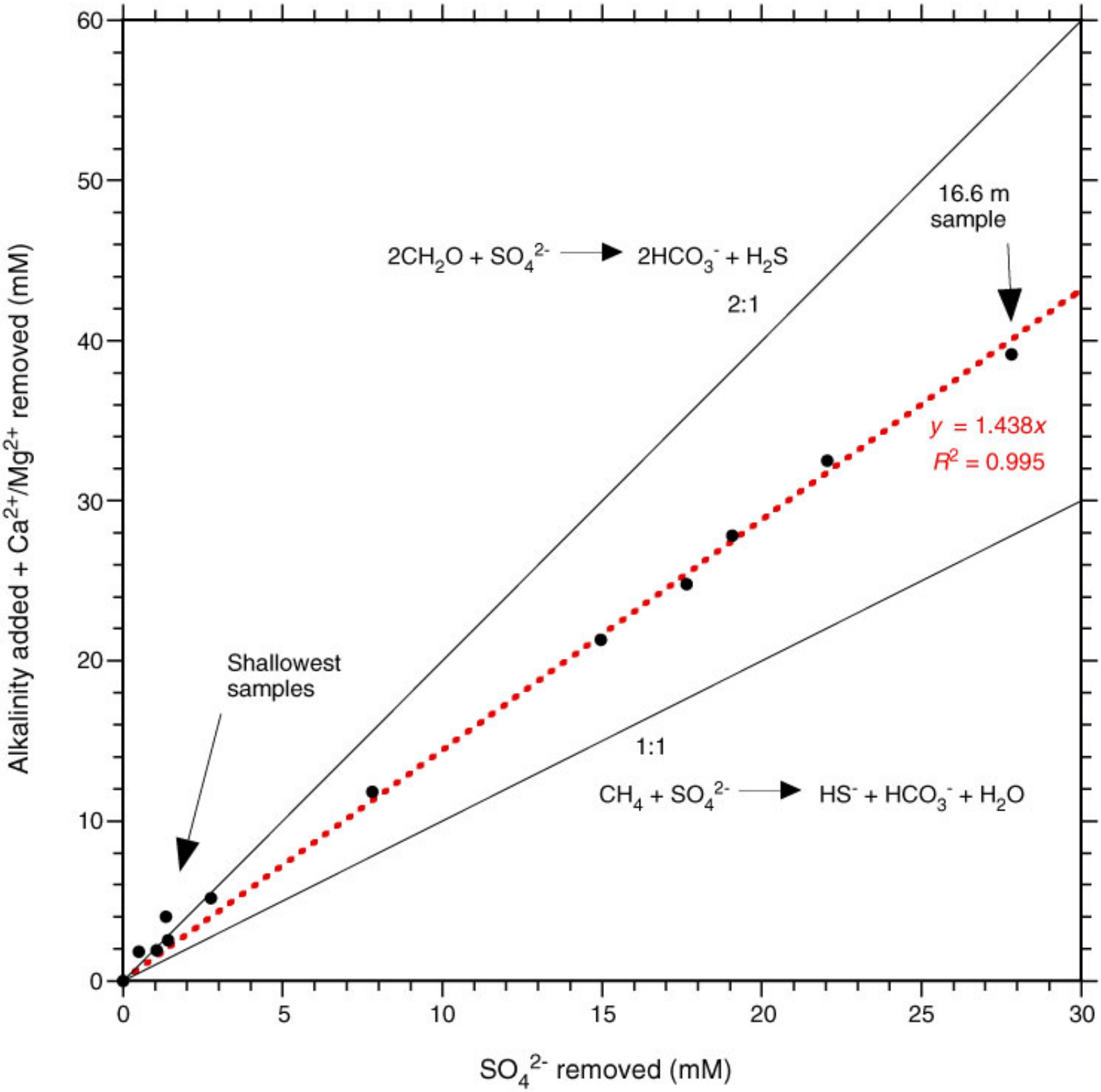
Alkalinity added + Ca^{2+}/Mg^{2+} removed (mM)
SO_4^{2-} removed (mM)
0
10
20
30
40
50
60
0
5
10
15
20
25
30
$2CH_2O + SO_4^{2-} \rightarrow 2HCO_3^- + H_2S$
2:1
16.6 m sample
$y = 1.438x$
$R^2 = 0.995$
Shallowest samples
1:1
$CH_4 + SO_4^{2-} \rightarrow HS^- + HCO_3^- + H_2O$

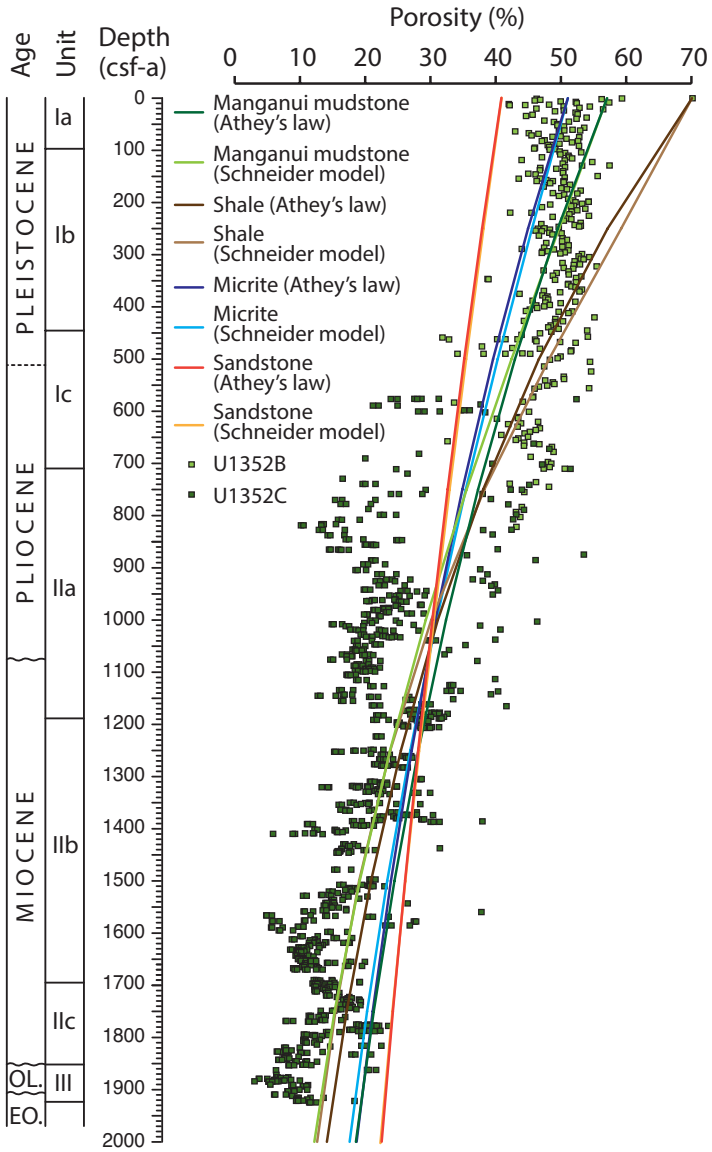
Age
Unit
Depth (csf-a)
Porosity (%)
0
10
20
30
40
50
60
70
PLEISTOCENE
PLIOCENE
MIOCENE
Ia
Ib
Ic
IIa
IIb
IIc
III
OL.
EO.
0
100
200
300
400
500
600
700
800
900
1000
1100
1200
1300
1400
1500
1600
1700
1800
1900
2000
Manganui mudstone (Athey's law)
Manganui mudstone (Schneider model)
Shale (Athey's law)
Shale (Schneider model)
Micrite (Athey's law)
Micrite (Schneider model)
Sandstone (Athey's law)
Sandstone (Schneider model)
U1352B
U1352C

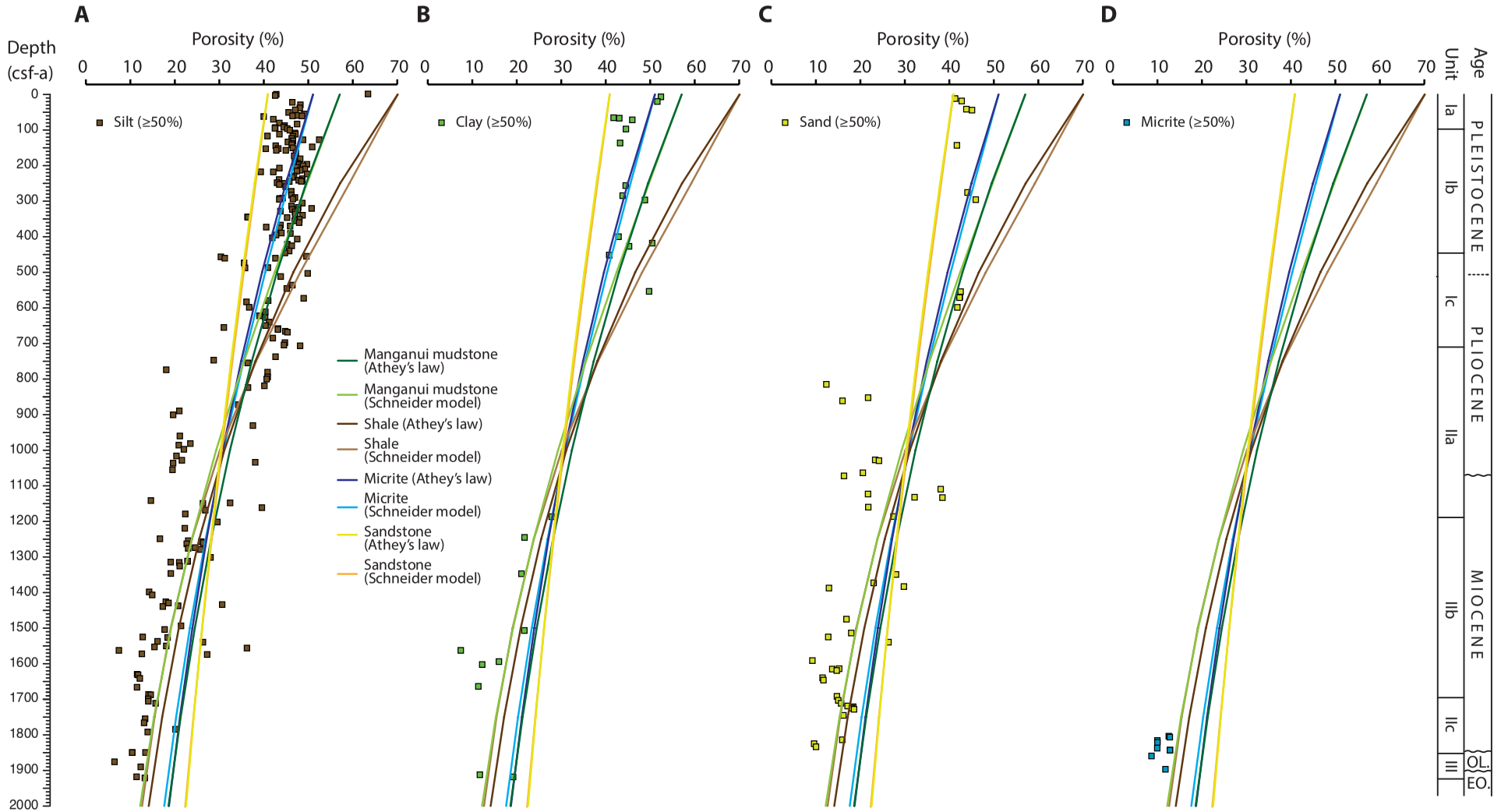
A
B
C
D
Depth (csf-a)
Porosity (%)
0 10 20 30 40 50 60 70
0 100 200 300 400 500 600 700 800 900 1000 1100 1200 1300 1400 1500 1600 1700 1800 1900 2000
Silt (≥50%)
Clay (≥50%)
Sand (≥50%)
Micrite (≥50%)
Manganui mudstone (Athey's law)
Manganui mudstone (Schneider model)
Shale (Athey's law)
Shale (Schneider model)
Micrite (Athey's law)
Micrite (Schneider model)
Sandstone (Athey's law)
Sandstone (Schneider model)
Age
Unit
Ia
Ib
Ic
IIa
IIb
IIc
III
PLEISTOCENE
PLIOCENE
MIOCENE
OL.
EO.